THESIS

DRIVERS OF STREAM CHANNEL EROSION AND DEPOSITION IN POST-FIRE WATERSHEDS

Submitted by

Alexander Thornton-Dunwoody

Department of Civil & Environmental Engineering

In partial fulfillment of the requirements

For the Degree of Master of Science

Colorado State University

Fort Collins, Colorado

Summer 2025

Master's Committee:

Advisor: Peter Nelson

Stephanie Kampf
Frances Davenport

ABSTRACT

DRIVERS OF STREAM CHANNEL EROSION AND DEPOSITION IN POST-FIRE WATERSHEDS

Wildfires alter watershed hydrology and sediment dynamics, yet the relative importance of topographic, climatic, and vegetation controls on channel erosion remains poorly quantified. This study investigates the primary physical controls influencing channel erosion and following the Cameron Peak Fire (CPF) and East Troublesome Fire (ETF) in northern Colorado. Geomorphic change was quantified using digital elevation models of difference (DoDs) derived from structure-from-motion and LiDAR data, covering both cumulative (2023 – 2021/2020) and delayed (2023 – 2022) post-fire periods. Spatial stream network (SSN) models were applied to assess the influence of topographic, climatic, vegetation, and soil variables across hillslope, channel, and watershed scales.

Results show that watershed and channel slopes were the strongest and most consistent predictors of both erosion and deposition. In contrast, stream power and drainage area exhibited site-specific and time-dependent effects. In CPF watersheds, high-intensity, short-duration storms increased sediment flux, whereas precipitation played a negligible role in ETF. Vegetation and soil variables—NDVI, clay content, and burn severity—were weak or inconsistent predictors across models. These results underscore the primacy of topographic controls, particularly slope, over other commonly cited drivers, and suggest that post-fire erosion risk is more strongly associated with terrain steepness than with burn severity.

ACKNOWLEDGEMENTS

I would like to thank the Colorado Water Conservation Board and Northern Water for their generous support, which made this research possible. Special thanks to the Coalition for the Poudre River Catchment, the City of Greeley, and the USDA Agricultural Research Service for their contributions to this project.

I am deeply grateful to my advisor, Peter Nelson, for his patience, insight, and steady guidance throughout my graduate studies. Thank you also to my committee members, Stephanie Kampf and Frances Davenport, whose feedback has been invaluable.

Many thanks to Mitch Delcau for assistance with data collection, Phoebe White and Megan Sears for providing insight on working with MRMS precipitation data, and Lindsey Hayter and Johnny Murray, whose previous work provided a foundation for this thesis.

Finally, heartfelt appreciation goes to the supportive community I've found in Fort Collins, my family for their support, and especially to my lovely wife Brenna, whose encouragement and humor have buoyed my spirit.

TABLE OF CONTENTS

1. INTRODUCTION

1.1 Background

Wildfire triggers a cascade of geomorphic and hydrologic responses that begin at the hillslope and propagate downstream to the river corridor. When a wildfire burns through an undeveloped catchment, it removes the protective cover of vegetation and litter that normally intercepts rainfall, dissipates the energy of raindrops, and maintains surface roughness (Bradford et al., 1987; L. DeBano et al., 1998). Without this protective shield, raindrops strike the bare soil directly, transferring kinetic energy that disrupts soil aggregates and accelerates the detachment of particles (L. DeBano et al., 1998; Robichaud et al., 2000). Moreover, moderate- to high-severity fires not only strip away vegetation but also alter the soil's structure by combusting organic matter and breaking down mineral bindings (Fernández et al., 2010; Larsen & MacDonald, 2007). These processes often lead to reduced infiltration, the development of water-repellent soil layers (Doerr & Thomas, 2000), and even the formation of impermeable crusts (Silva et al., 2019). The consequences of these changes are profound. Post-fire hydrophobicity limits soil infiltration and intensifies runoff, which accelerates interrill and rill erosion (Rengers et al., 2016) and promotes debris flows (Cannon & DeGraff, 2009; Vieira et al., 2015). Furthermore, dry ravel processes are often intensified after wildfire, contributing sediment directly to headwater streams (Jackson & Roering, 2009).

However, even in severely burned watersheds, fire alone does not always cause large geomorphic changes channels (Owens et al., 2013; Prosser, 1990). The magnitude of geomorphic response channels after fire also depends on changes in process rates that, in addition to burn severity, are controlled by interactions between topography, vegetation, soil and geological factors, the local history of disturbance and precipitation regime on the hillslope and channel

scales (Kampf et al., 2016; McGuire et al., 2024; Vieira et al., 2015; Wagenbrenner et al., 2021; Wilson et al., 2018).

Vegetation and soil characteristics modulate hillslope erosion by governing erosivity—the erosive force of rainfall and runoff—and erodibility—the soil's resistance to erosion. Post-fire reduction in vegetation destabilizes hillslopes and increases susceptibility to gully erosion (Goode et al., 2012; Istanbulluoglu & Bras, 2006; Kirkby & Cox, 1995; Langbein & Schumm, 1958). Additionally, wildfire impacts soil structure and hydrology variably depending on soil texture and organic content, with fine, organic-rich soils typically becoming more hydrophobic and prone to erosion as fire volatilizes organic compounds that condense on cooler soil surfaces, forming a water-repellent layer (L. F. DeBano, 1981; Shakesby, 2011). Outside the context of wildfire, inherent soil erodibility is strongly influenced by texture and composition—soils high in silt, low in clay, and poor in organic matter tend to be the most erodible due to weaker aggregate formation. (Wischmeier & Mannering, 1969).

Precipitation regimes in the intermountain western U.S. primarily drive episodic post-fire geomorphic events through high-intensity convective storms that induce infiltration-excess runoff on hillslopes (Benavides-Solorio & MacDonald, 2005). Short-duration, high-intensity rainfall events are especially critical in generating significant sediment yields and flooding events post-fire (Inbar et al., 1998; Lane et al., 2006; Moody & Martin, 2001; Murphy et al., 2015). Many studies focusing on rainfall conditions leading to post-fire geomorphic responses have been developed in recent decades, with some metrics focused on maximum intensity rainfall over a 10, 30 or 60 minute period (Kampf et al., 2016; Wilson et al., 2018) and others focusing on a thresholded cumulative rainfall, or “storm accumulation” (Esposito et al., 2023).

Topographic factors besides slope also significantly impact erosion. Relief, drainage density, and basin area influence runoff concentration and sediment dynamics, with high-relief areas fostering concentrated flow networks and greater incision potential (Horton, 1945; Melton, 1957). Rills and gullies have been found to develop on hillslopes once runoff exceeds a critical combination of slope and contributing area, with steeper slopes generally eroding larger volumes of sediment (Montgomery & Dietrich, 1989; Patton & Schumm, 1975). Increased hillslope length further enhances runoff concentration and shear stress, amplifying soil loss (Moore & Burch, 1986). Elevated hillslope drainage density, indicating a higher abundance of rills and gullies, is associated with more efficient sediment transport networks (Moody & Kinner, 2006; Staley et al., 2010). Hillslope profile curvature additionally influences how sediment is delivered to the valley, with convex profiles accelerating flow and erosion, while concave profiles reduce runoff velocities, promoting deposition (Rieke-Zapp & Nearing, 2005).

Collectively, these processes result in episodic sediment pulses moving from hillslopes into channels via landslides, debris flows, and gully erosion (Cannon & DeGraff, 2009; Moody et al., 2008). Such episodic sediment delivery is integral to long-term erosion dynamics in Rocky Mountain basins, where headwater channels periodically accumulate and subsequently evacuate sediment through mechanisms like debris flows and gullies (Benda et al., 2003; E. E. Wohl & Pearthree, 1991). These sediment accumulations are encouraged by headwater channel characteristics, including limited drainage areas, stepped longitudinal profiles, elevated surface roughness, and cohesive sediment properties (Benda et al., 2003). Wildfire impacts can transition these headwater streams from supply-limited to transport-limited states (Moody, 2001). The magnitude of these effects has been found to be closely linked to burn severity: more intense fires lead to greater soil degradation and, consequently, a heightened erosional response both on

the hillslope and the catchment scale (McGuire et al., 2024; Vieira et al., 2015; Wagenbrenner et al., 2021).

Empirical studies emphasize watershed morphology as a foundational control on sediment transport and channel erosion. Within channels, steeper reaches exhibit higher velocities and shear stresses that mobilize coarser material and drive bed and bank incision until a graded equilibrium is attained (Bull, 1979; Leopold & Maddock, 1953). Prior work has shown that stream-power and gradients in stream power can effectively model channel dynamics to predict whether a reach will erode or aggrade (Fuller, 2008; Gartner et al., 2014; Yochum et al., 2017). In scenarios without flow data, basin area has been used as a proxy in stream-power calculations to evaluate channel response (Rengers et al., 2021)

The impact of these variables at the channel, hillslope, and watershed scales on geomorphic change in the channel following wildfire is summarized in figure 1.

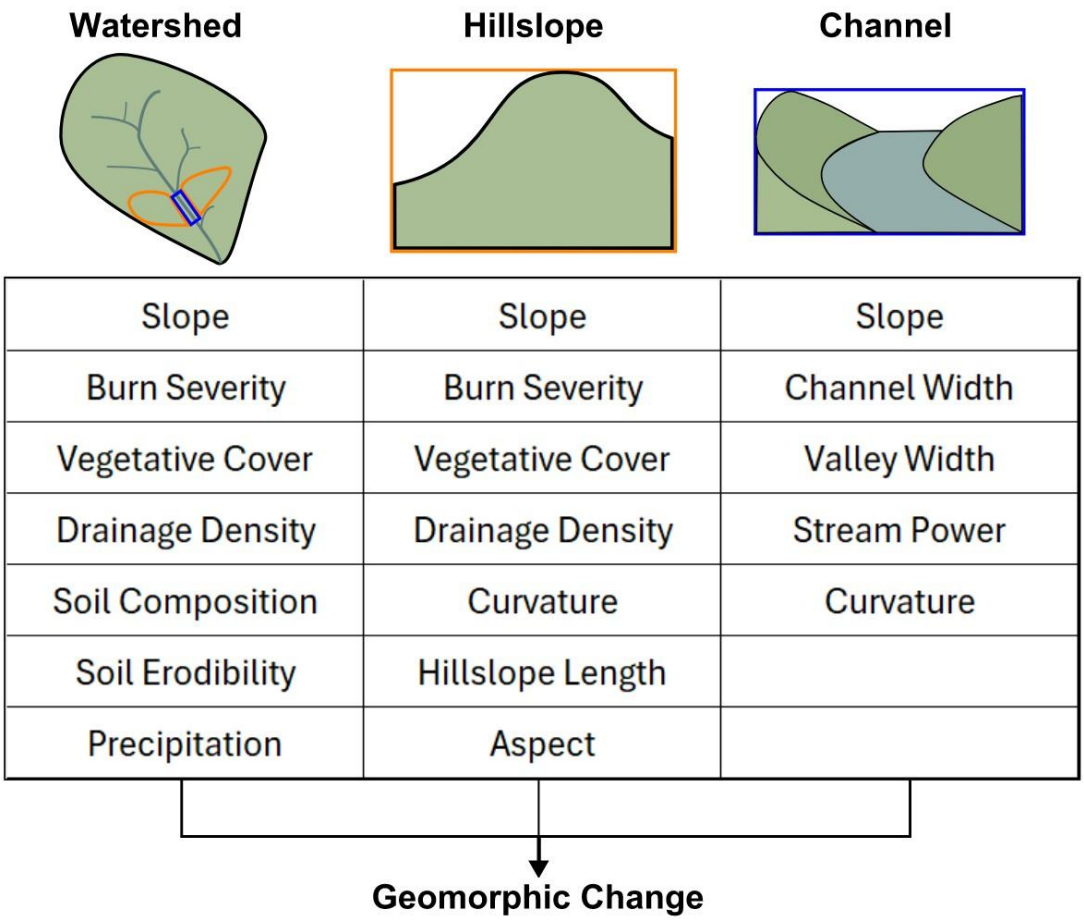

Figure 1: Topographic, geologic, vegetative, and climatic factors influence geomorphic change at the watershed, hillslope, and channel scales.

1.2 Research Questions

The primary objective of this study is to evaluate which physical controls most significantly influence geomorphic response to wildfire. In the Fall of 2020, the CPF burned approximately 209,000 acres northwest of Fort Collins, Colorado and the ETF burned approximately 194,000 acres north of Grandby, Colorado, with both fires resulting in predominantly moderate to low burn severity (US Forest Service, 2020a, 2020b). A statistical analysis was undertaken to assess geomorphic change in the channel and answer the following questions:

1. Which environmental factors operating at the channel, hillslope, and watershed scales exert the strongest influence on post-wildfire geomorphic changes in the channel network and how do the relative contributions of these factors vary among different burn scars?
2. How do the relative influences of precipitation, burn severity, vegetation, soil properties, and topography on channel erosion differ between the cumulative post-fire period (2023 – 2021/2020) and the delayed post-fire period (2023 – 2022)?

2. METHODS

To address the research questions above, high-resolution digital surface models (DSMs) were generated using structure-from-motion (SfM) surveys across five sites in the Cameron Peak Fire (CPF) and three sites in the East Troublesome Fire (ETF) burn scars during 2022 and 2023. Pre-fire (ETF, 2020) and post-fire (CPF, 2021) LiDAR-derived digital elevation models (DEMs) were integrated into the analysis. Vegetation pixels were masked from SfM DSMs to produce bare-earth SfM DEMs, which were co-registered with the LiDAR DEMs. Geomorphic change was quantified using DEMs of Difference (DoDs) for erosion (delayed interval, 2023–2022 and cumulative interval 2023–2021/2020) and deposition and net change (delayed interval 2023–2022 only), including associated 95% confidence intervals. Predictor variables related to topography, geology, vegetation, and climate were aggregated at watershed, hillslope, and channel scales, and analyzed using generalized linear mixed models (GLMs).

2.1 Study Sites

This study encompasses sites from both the Cameron Peak Fire (CPF) and the East Troublesome Fire (ETF) burn scars in Northern Colorado. (Figure 2). Some of the watersheds in both the burn scars were mulched as an emergency erosion mitigation measure, but previous studies

found that the mulching had no effect on geomorphic change in the watersheds (Hayter, 2023; Murray, 2023). In the CPF burn scar, we selected five adjoining catchments—two mulched (CPF-ME, CPF-MM) and three unmulched (CPF-UE, CPF-UM, CPF-UW)—that drain northeast into Bennett Creek and have drainage areas ranging from 0.57 to 1.49 km². Elevations span from 2,342 to 2,779 m, with mean slopes of 14.2 to 15.8 degrees. These catchments experienced primarily moderate burn severity, with high-severity patches concentrated around channel networks. Vegetation prior to burning comprised ponderosa pine (Pinus ponderosa), Douglas-fir (Pseudotsuga menziesii), lodgepole pine (Pinus contorta), and a diverse understory of shrubs and grasses (Chapman et al., 2006). Geology consists mainly of biotite granite and schist (Workman et al., 2018). Soils are classified as Cypher-Ratake and Bullwark-Catamount family complexes— very cobbly to gravelly sandy loams that are excessively to well-drained types—with frequent interspersed rock outcrops (NRCS, 2021). Channels are characterized by step pools formed by large wood, with low, steady flows from groundwater and brief stormflows during summer thunderstorms. Streamflow for each catchment is dependent on drainage area; ME and UW are perennial while flow in the smaller watersheds, MM, UE, and UM, is intermittent depending on precipitation and groundwater seeps.

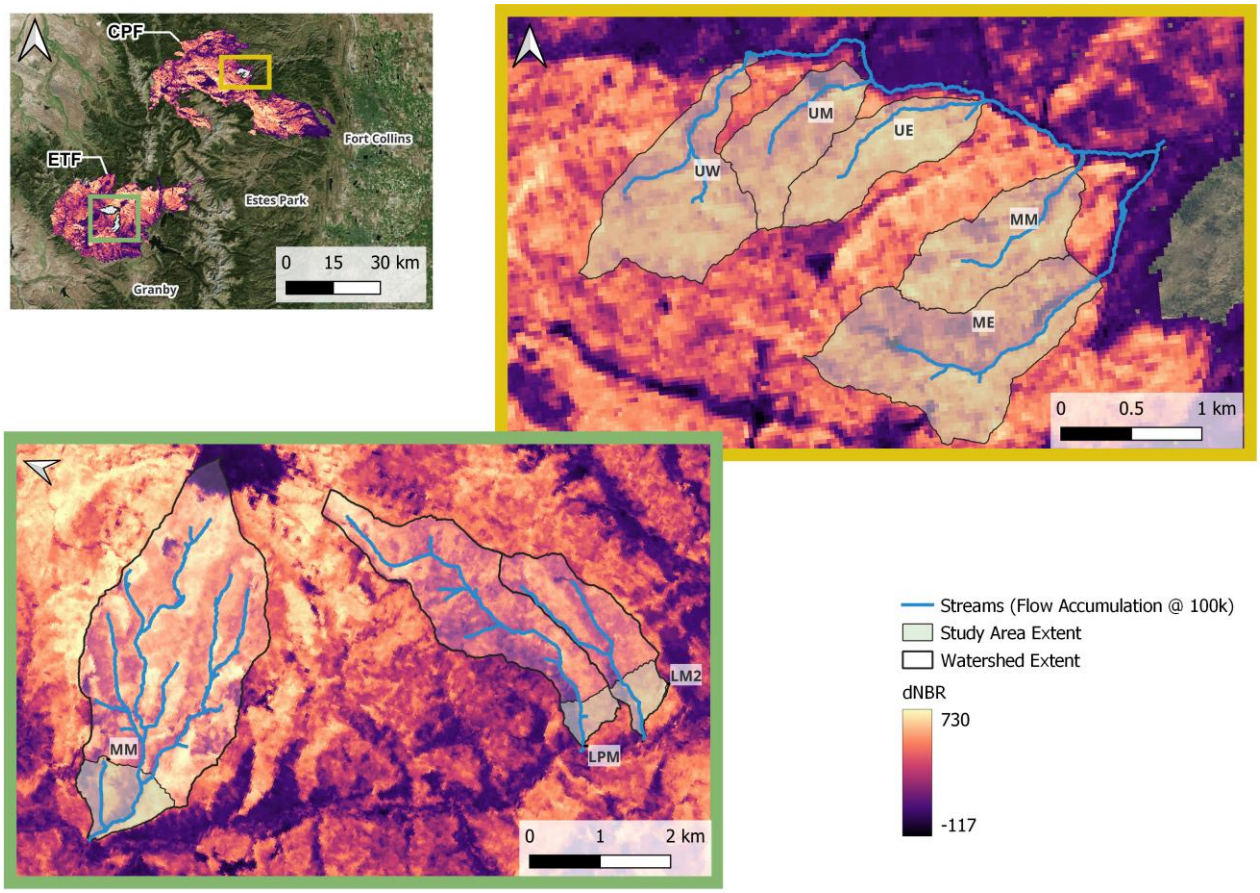

Figure 2. Study sites and associated watersheds, with the difference in normalized burn ratio (dNBR) overlain.

The ETF study area includes three tributaries, with two lower elevation areas (ETF-LM2, ETF-LPM) and one middle elevation area (ETF-MM), with elevations ranging from 2,559 to 3,495 m. In the ETF study areas, access constraints due to extreme topography and flash flooding restricted data collection to lower watershed areas, which ranged in size from 0.61 to 1.44 km². The contributing drainage areas for these channel segments ranged from 2.23 to 9.18 km^2. All study areas drain directly into Willow Creek. The outlet of LPM is a large fan of unconsolidated material that was likely deposited by historical debris flow activity. Burn severity across the ETF sites was largely moderate to high, resulting in substantial vegetation loss and ground debris.

ETF sites fall within sedimentary mid-elevation and subalpine forest ecoregions, with dominant vegetation including lodgepole pine, grouse whortleberry, subalpine fir, Engelmann spruce, russet buffaloberry, and diverse shrub and grass groundcovers (Chapman et al., 2006; NRCS, 2021). Geologic substrate primarily includes sandstone-based Frisco, Howlett, and Scout family moist complexes (NRCS, 2021). Annual precipitation is highly variable, predominantly as winter snowfall and intense localized convective summer storms.

Sites in both the CPF and ETF burn scars have a semi-arid climate, with annual precipitation ranging from 400 mm to 500 mm, primarily from winter snow and summer convective thunderstorms (PRISM Climate Group, n.d.).

Topographic, vegetation, and precipitation characteristics are summarized in Table 1 below.

Table 1. Summary of site characteristics within the ETF and CPF burn scars. The mean normalized difference in vegetation index (NDVI) reflects average values during snow free months (June -October) between the time of the fire and the 2023 survey date. NDVI was derived from Planet Labs imagery using the red and near-infrared bands, with approximately 3-week intervals between satellite images. The 10-min Storm Accumulation Mean is the average rainfall total from events exceeding an intensity of 10 mm/hour over a 10 minute period, based on 2-minute MRMS QPE precipitation intensity rasters with a spatial resolution of 1 kilometer.

Burn Scar	Study Site	Study Area (km^2)	Basin Area (km^2)	Elevation Min (m)	Elevation Max (m)	Slope Mean (degrees)	10-min Storm Accumulation Mean (mm)	dNBR Mean	NDVI Mean
CPF	ME	1.35	1.35	2387	2682	14.8	539.5	449.7	0.34
	MM	0.72	0.72	2342	2640	15.8	522.9	508.3	0.32
	UE	0.62	0.62	2368	2650	14.8	553.2	578.7	0.32
	UM	0.57	0.57	2404	2653	14.3	565.4	458.4	0.35
	UW	1.03	1.03	2453	2781	14.2	588.4	481.5	0.31
ETF	LM2	0.61	2.23	2560	3010	17.5	218.8	425.8	0.38
	LPM	0.65	4.46	2559	3330	21.4	264.1	418.8	0.39
	MM	1.14	9.18	2625	3495	16.7	318.2	555.6	0.37

2.2 Data Collection

CPF and ETF surveys were collected using two drones: the WingtraOne Gen II fixed-wing (Wingtra) drone and the DJI Phantom 4 RTK (DJI) drone. Both drones can be pre-programmed to collect surveys autonomously and follow a set of input parameters specified during flight planning. The Wingtra drone is equipped with a 42MP Sony RX1R II camera and was programmed to fly at 120 m above ground level (relative to the USGS 1/3 arc-second Digital Elevation Model) with a 70% side and front photo overlap, corresponding to a ground sampling distance (GSD) of 1.6 cm per pixel. The DJI drone is equipped with a 1-inch 20MP CMOS mechanical shutter camera and was programmed to fly at 100 m above ground level with a 70% side and 80% front overlap, which resulted in a GSD of 2.7 cm per pixel.

A DJI D-RTK2 base station setup over a known ground control point was used to communicate with the RTK GNSS module on board the DJI drone, while a Topcon GR-5 GNSS base station was to correct the coordinates provided by the PPK GNSS module on board the Wingtra. The receiver was set up no more than 1 km from the take-off location for the drone and collected static data at 1-second intervals for at least one hour including during the flight. Static positioning data from the base station were corrected with NOAA's Online Positioning User Service (OPUS), which references observations to the National Spatial Reference System (NSRS) with typical accuracies of a few centimeters. The Wingtra is equipped with an onboard high-precision post processed kinematic (PPK) global navigation satellite system (GNSS) module, which meant it was not necessary to use ground control points (GCPs) to georeference images during post-processing (de Haas et al., 2021).

CPF surveys were conducted in May 2022 with the DJI drone and June 2023 with the Wingtra drone. ETF surveys were flown between September 2022 and July 2023 using the Wingtra drone

(Table 2). The OPUS corrected, PPK processed images had vertical and horizontal errors that ranged from <1 to 5 cm.

Table 2. Survey dates for each study area. *Survey showed alignment issues and was disregarded from analysis

Burn Scar	Study Area	Survey Date	Survey Type
CPF	ME	9/8/2021*	LiDAR
		6/4/2022	SfM
		5/31/2023	SfM
	MM	9/8/2021	LiDAR
		5/8/2022*	SfM
		5/31/2023	SfM
	UE	9/8/2021	LiDAR
		5/11/2022	SfM
		5/31/2023	SfM
	UM	9/8/2021	LiDAR
		6/1/2022	SfM
		5/31/2023	SfM
	UW	9/8/2021	LiDAR
		6/9/2022	SfM
		5/31/2023	SfM
ETF	LM2	9/4/2020	LiDAR
		8/12/2022	SfM
		7/9/2023	SfM
	LPM	9/6/2020	LiDAR
		8/12/2022	SfM
		7/9/2023	SfM
	MM	10/4/2020	LiDAR
		9/1/2022	SfM
		7/9/2023	SfM

The images were processed using Agisoft Metashape with a structure-from-motion (SfM) workflow to generate dense point clouds, digital elevation models (DEMs), and orthomosaics for each flight. SfM enables the reconstruction of 3D topography from overlapping 2D images with location data. A major challenge with repeat surveys is ensuring accurate and consistent

alignment of output digital surface models (DSMs). To address this, we followed the USGS workflow described by Over et al. (2021) and applied a coregistration method during SfM optimization (Cook & Dietze, 2019) that identifies common tie points in stable areas to minimize relative uncertainty between flights.

Images from all flights over each watershed were processed together in a single chunk in Agisoft Metashape, with camera locations enabled only for the flight with the lowest reported geotagging error. These reference images guided the alignment, tie point detection, and optimization. Since the 2022 CPF survey was flown with the DJI drone without PPK correction, the images from the 2023 CPF surveys were used as a reference. After optimization, images were divided into separate chunks by flight date, and the final point clouds, DSMs, and orthomosaics were generated and exported. To provide a common resolution for equal comparison across watersheds, DEMs were all exported at a resolution of 10 cm, and orthomosaics were exported at a resolution of 4 cm.

2.3 Vegetation Masking and LiDAR DEM Co-registration

The workflow developed to mask the SfM DEMs and co-register them with the LiDAR DEMs is detailed in Appendix A. Vegetation presents a major challenge for detecting geomorphic change using SfM-derived DEMs. In contrast to LiDAR surveys which can penetrate the vegetation canopy, SfM produces a digital surface model (DSM) that captures both ground and vegetation surfaces. When DSMs are differenced to detect change, vertical changes in vegetation growth or loss can be conflated with vertical changes due to erosion and deposition. Although LiDAR better penetrates vegetation, the presence of dense vegetation can still increase vertical error in LiDAR-derived elevation data (Brogan et al., 2019). To address this problem, we used a random forest classifier to classify vegetation pixels in each DSM using the red-green-blue (RBG)

orthomosaic imagery and a roughness raster, which is calculated by the largest inter-cell difference of a central pixel in the DSM and its surrounding cells. Training and validation polygons were manually delineated using the orthomosaic to distinguish between water, vegetation, downed logs (burned and unburned), and bare earth. The resulting classification raster was then used to remove any SfM raster pixels classified as water, vegetation, or downed logs.

Accurate quantification of geomorphic change using a DEM of Difference (DoD) requires precise spatial alignment between SfM- and USGS LiDAR-derived elevation models. However, achieving this alignment remains challenging, as misalignments commonly persist despite adherence to best practices in SfM processing. These discrepancies can introduce significant error into change detection analyses. (Chirico et al., 2020; Hugonnet et al., 2021; Niculiță et al., 2020). The error in alignment between these two datasets can be minimized through DEM co-registration (Shean et al., 2016).

Airborne LiDAR DEMs were obtained from OpenTopography and had a resolution of 1 meter. The USGS 2020 LiDAR DEM (USGS, 2022a) was flown over the ETF study sites between September and October 2020, immediately prior to ETF. The USGS 2021 LiDAR DEM (USGS, 2022b) was flown over the CPF study sites in September 2021, approximately 1 year after the CPF burned through the study sites. Both the 2023 and 2022 SfM surveys were co-registered to their respective LiDAR datasets. However, due to inadequate alignment between the 2022 SfM data and the 2021 LiDAR in the CPF study area, the 2023 SfM surveys were selected as the primary dataset for alignment with the 2021 and 2020 LiDAR DEMs.

2.4 Geomorphic Change Quantification

Horizontal errors in both the LiDAR and SfM surveys were significantly smaller than vertical errors and were therefore excluded from the DoD error analysis. Vertical errors were more substantial and comprised both systematic and random components (James et al., 2020). Systematic vertical errors (e.g. 'doming, $p < 0.1$) typically result from issues like inaccurate camera calibration, insufficient variation in camera angles, excessive shadows in the aerial photos, or a lack of PPK correction, all of which lead to vertical distortions in the reconstructed surface (Clark et al., 2021; M. James et al., 2017; M. R. James & Robson, 2014). Visual inspections for doming in the DoDs and evaluations of the magnitude of change on stable surfaces (e.g. roads and ridge lines) indicated no detectable systematic error across all study areas.

Random error, which reflects measurement precision, originates during SfM image processing steps such as tie point matching and optimization (James et al., 2020). To quantify spatially variable random errors we applied the workflow outlined by James et al. (2020): precision estimates (as XY points) were extracted from Agisoft Metashape for each DEM and then gridded using the Surfer kriging tool from Golden Software, LLC (Surfer Software) into a raster with a 10 cm resolution. We propagated these DEM random errors to the DoD under the assumption that errors are Gaussian and independent between the two surveys (Brasington & Smart, 2003), with δ_{DoD} representing the 95% confidence interval of the propagated error and δ_{DEM_1} and δ_{DEM_2} corresponding to the random errors from the two DEMs being differenced.

$$\delta_{\mathrm{DoD}} = \pm 1.96\sqrt{\delta^2_{\mathrm{DEM}_1} + \delta^2_{\mathrm{DEM}_2}} \quad (1)$$

Thresholding is essential for accurately quantifying gross geomorphic changes, such as total erosion (sum of negative elevation changes) and total deposition (sum of positive elevation changes), as these measures are systematically biased by random errors present even in geomorphically stable regions of the DEM (Anderson, 2019). Thus, only DoD values exceeding δ_{DoD} were included in gross erosion and deposition calculations. All DoD values were retained in net geomorphic change calculations, as net change is relatively insensitive to random error, and applying a threshold in this context can bias results and misrepresent uncertainty (Anderson, 2019).

To quantify volumetric uncertainty, we applied the statistical methods for propagating spatially correlated random errors presented in Rolstad et al. (2009) by converting each unfiltered DoD to points and performing a semi-variogram analysis. Using Surfer Software, a spherical semi-variogram model with no nugget was generated to obtain the DoD's semi-variance and range. Volume uncertainty was then calculated using the error propagation formula:

$$\sigma_v = \pm 1.96\, L\, \sigma_{sc}\, \alpha_i \sqrt{\frac{n\,\pi}{5}} \quad (2)$$

where n is the number of cells, L is the cell size, σ_{sc} is the square root of the semi-variance at the sill, and α_i is the fitted range. Finally, σ_{sc} was multiplied by 1.96 to report estimates at the 95% confidence interval (Anderson, 2019).

We manually delineated channel polygons in each study area by visually interpreting a combination of Structure-from-Motion (SfM) orthomosaic imagery and slope rasters. For the statistical analysis, the channel needs to be divided into segments over which erosion and deposition will be aggregated. The choice of segmentation interval is arbitrary: longer intervals yield segments with more pixels capturing geomorphic change but reduce the total segment

count. Following an evaluation of predictive accuracy for channel segmentation intervals of 5, 10, and 20 meters, channels were segmented at 10-meter intervals for this study (*see Section 2.6 and Appendix C*). Within each polygon segment, mean and total values of erosion and deposition were computed from vegetation-masked and error-thresholded rasters, while mean and total net elevation change were calculated from vegetation-masked rasters alone. Cumulative volumetric uncertainties for erosion, deposition, and net change along channel networks were obtained by summing σ_v values for the current segment and all upstream segments, yielding cumulative 95% confidence intervals (Anderson, 2019).

2.5 Spatial Stream Network Models

Geomorphic change in the channel was modeled using spatial stream network (SSN) models implemented via the SSN2 package in R (Dumelle et al., 2024; Ver Hoef et al., 2014). SSN models—first developed by Ver Hoef and Peterson (2010)—are a subclass of generalized linear models incorporating network-specific covariance structures (e.g., tail-up and tail-down) to explicitly account for spatial autocorrelation in stream data (Ver Hoef & Peterson, 2010). Unlike standard spatial generalized linear mixed-models (GLMs) that impose Euclidean covariance on residuals, SSN models use hydrologically-constrained covariance functions within a mixed-effects framework, improving parameter inference (Ver Hoef et al., 2014). The resulting model partitions total variance into (1) that explained by fixed predictors, (2) that explained by spatial autocorrelation along the channel network (e.g. adjacent segments have similar levels of geomorphic change), (3) that explained by spatial autocorrelation independent of the channel network (e.g. adjacent watersheds have similar levels of geomorphic change) and (4) that explained by additional random effects (e.g., study area grouping).

Developing SSN models requires constructing a topologically accurate digital stream network to calculate hydrological contributions and spatial weights for each stream reach and corresponding sample location. For this study, we generated a synthetic stream network from USGS 1-meter LiDAR-derived DEMs using Whitebox Tools (Lindsay, 2014). Stream network topology validation, integration of sampling points into the network geodatabase, and computation of hydrological distances among sampling locations were conducted with the SSNbler R package (Peterson & Pearse, 2024).

Following selection of explanatory variables (*see Section 2.6)*, SSN models were constructed by first identifying the optimal autocorrelation structure. We systematically compared all possible combinations of the euclidean and stream network autocorrelation structures and their associated averaging functions, selecting the optimal model based on the Akaike Information Criterion (AIC) weight (Burnham et al., 2010) and root mean squared error (RMSE) of the leave one out cross validation (LOOCV). The optimal autocorrelation structure for the ETF-combined model included a *linear* tail-up model, a *spherical* tail-down model, and no Euclidean or nugget components. This optimal structure was then applied consistently to all subsequent ETF and CPF models.

For this study, we built models for each individual study area in the ETF and CPF burn scars, as well as combined models for each burn scar (ETF-combined and CPF-combined). The individual models incorporated only independent variables, while the combined models included a random effects term to account for the additional covariance introduced by differences among watershed areas. Erosion and deposition were modeled using a generalized linear model with a Gamma distribution link function, reflecting the skewed distribution of these variables, whereas net

change was modeled using a linear model with a Gaussian distribution due to its near-normal distribution.

Model evaluation was conducted to evaluate whether key statistical assumptions underlying the analysis were satisfied, thereby ensuring the reliability of the model results. Specifically, model residuals were assessed visually using three diagnostic plots: (1) a quantile-quantile (Q-Q) plot to evaluate residual normality, (2) a plot of residuals against fitted values to detect heteroscedasticity, and (3) a histogram of residuals to further examine their distribution. Methods followed recommendations described by Zuur et al. (2010). Residuals ideally exhibit linearity in the Q-Q plot, randomness in the residuals versus fitted values plot, and approximate symmetry in the histogram, collectively indicating compliance with assumptions of normality, homogeneity of variance, and minimal spatial dependency after the incorporation of spatial covariance structures.

2.6 Model Terms

We characterized potential predictors using a suite of 18 variables capturing topography, climate, and burn severity (Table 3). These variables were summarized across three distinct spatial domains: channels, hillslopes, and watersheds. Each variable was aggregated as a mean, median, or percentage, as explicitly indicated by variable suffixes. The spatial domain for each variable is denoted by prefixes: "ch_" for channel-scale variables, "hs_" for hillslope-scale variables, and "ws_" for watershed-scale variables.

Channel segment polygons were converted into centroid points to serve as sampling locations for SSN modeling. From each sampling point, upstream watershed areas were delineated using Whitebox Tools. Variables summarized across these upstream watershed polygons were assigned the "ws_" prefix. Hillslope polygons, representing the local hillslope influence area,

were defined by differencing the contributing area polygon of the next upstream sampling location from the contributing area polygon of the current sampling location. Variables aggregated within these hillslope polygons were labeled with the "hs_" prefix. Variables with the “central_diff” suffix represent how explanatory variables are changing through the channel, and are computed by the difference of the downstream sampling location value minus the upstream sampling location value.

Multi-Radar/Multi-Sensor (MRMS) data sources included hourly Multi-Sensor Quantitative Precipitation Estimation (QPE) and radar-only QPE products, alongside the Surface Precipitation Rate (SPR), a raw radar product available at 2-minute intervals. A correction factor was derived by evaluating the relationship between SPR and QPE values and subsequently applied to the SPR dataset, yielding adjusted precipitation rates at 2-minute resolution. Precipitation was then aggregated into 10-minute storm accumulations by summing corrected MRMS raster cells with precipitation intensities exceeding a threshold of 10 mm/hr for a minimum of 10 minutes. A rolling sum was used to identify time steps where precipitation exceeded the threshold, generating a Boolean mask. Original 2-minute precipitation values within these intervals were then summed, resulting in a raster dataset representing accumulated precipitation for all storm events surpassing the 10 mm/hr intensity threshold. The 10 mm/hr threshold was selected based on prior work demonstrating that sediment yield and geomorphic change in post-fire landscapes in the Northern Colorado Rockies correlate strongly with rainfall intensities exceeding 10–30 mm/hr (Kampf et al., 2016)

Vegetation was assessed using the Normalized Difference Vegetation Index (NDVI), calculated from Planet Labs satellite imagery with a spatial resolution of 3 meters. NDVI mean values were computed as an average of NDVI values at biweekly intervals from June through October from

the date of the initial survey to the final survey. Burn severity data were obtained from the Burned Area Emergency Response (BAER) differenced Normalized Burn Ratio (dNBR) product, which has a spatial resolution of 30 meters. The central difference of watershed drainage area represents confluences in the stream network, where higher values indicate larger tributaries joining the mainstem.

Figure 1 illustrates the delineation and hierarchical relationships of these three spatial domains.

We identified outliers in each dependent variable (erosion, deposition, and net change) as values exceeding 1.5 × IQR (Zuur et al., 2010), verified them against orthomosaic imagery, and excluded segments with clearly erroneous values. The histogram of each explanatory variable was assessed for distributional skewness, and skewed variables were log-transformed. Variables exhibiting pronounced non-normal spread were summarized by median rather than mean to limit outlier influence. To compare effect sizes in our SSN models, all predictors were standardized to z-scores (mean = 0, SD = 1) by subtracting each variable's sample mean and dividing by its sample standard deviation. The resulting unitless coefficients reflect the relative strength of association with geomorphic change (magnitude) and indicate directionality (sign).

Table 3. Descriptions of the explanatory variables used in the spatial stream network (SSN) models

Variable	Description	Resolution (m)	Source
10-min Storm Accumulation	A moving cumulative sum of rainfall for events exceeding 10 mm/hr.	1000	MRMS QPE 2-min rasters
BAER dNBR	Difference in normalized burn ratio one year after the fire	30	USDA BAER Maps
NDVI	Calculated from Planet 3-meter RGB-NIR imagery	3	Planet Labs Imagery
Clay	Percentage clay	2 - 6 km^2	NRCS Web Soil Survey
K_w	Soil erodibility factor	2 - 6 km^2	NRCS Web Soil Survey
Slope	Steepest rate of change in elevation	1	USGS LiDAR
Drainage Area	Flow accumulation from hydrologically corrected 1 m DEM	1	USGS LiDAR, Whitebox Tools
Drainage Density	$\frac{\text{Length of Stream Network}}{\text{Drainage Area}}$	1	Flow accumulation raster thresholded to 10,000 m^2
Hillslope Length	Length of hillslope segment	-	Maximum distance between two points on the hillslope polygon perimeter
Valley Width	$\frac{\text{Valley Segment Area}}{\text{Interval Width}}$	1	Valley Bottom Extraction Tool (Gilbert et al., 2016)
Channel Width	Width of active channel	-	Manually delineated by referencing SfM orthomosaic
Curvature	Profile curvature: the steepest rate of change of the slope	1	USGS LiDAR, Whitebox Tools
Stream Power	$\frac{\text{Slope} \times \text{Basin Area}}{\text{Channel Width}}$	-	(Rengers et al. 2021)
Central Difference	(value of downstream sampling location) – (value of upstream sampling location)	-	Computed in Python

We removed outliers from the dependent variables, log-transformed skewed explanatory variables, and standardized all predictors. We then assessed multicollinearity using variance inflation factors (VIF) and iteratively removed the predictor with the highest VIF until all VIFs were < 3. When any pair of remaining predictors correlated at $r > 0.7$, we excluded the variable

in that pair with the larger VIF (Zuur et al., 2017). We retained storm accumulation, valley width, hillslope dNBR, and slope at both channel and watershed scales in all models because these metrics represent the key controls on post-fire geomorphic response. In the individual models, only hillslope and channel-scale terms were included, because adding watershed-scale variables created linear dependencies among predictors (a rank deficiency in the design matrix), preventing unique estimation of regression coefficients.

Model performance was evaluated the SSN2 leave-one-out cross-validation (LOOCV) function, iteratively excludes a single observation and fits the model to the remaining data. Predicted values were extracted from posterior model fits, and differences between predicted and observed values were computed to determine normalized root mean squared error (nRMSE). nRMSE was calculated as the square root of the mean squared difference between observed and predicted values, divided by the mean value of the response variable. Normalizing RMSE by the response variable allows for a more direct comparison of performance between watersheds that have different magnitudes of geomorphic change. The SSN2 library also reports a "pseudo R^2" value for each model, which reflects the proportion of variability explained by the covariates, rather than serving as a direct measure of predictive performance.

3. RESULTS

3.1 Sediment Budgets

Cumulative channel erosion values for CPF study areas were generally lower magnitude than the mean erosion values for ETF study areas (Figure 3). The CPF-MM and CPF-UE watersheds show preferential erosion further upstream (i.e. smaller basin area), but the rest of the ETF and CPF study areas show no discernable trend between basin area and erosion. Figure C6 shows

generally higher magnitudes of deposition towards the mouth of ETF-LM2 and ETF-MM study areas, but the opposite trend in the ETF-LPM study area.

Overall, lower overall erosion was observed in the delayed ETF- (2023 – 2022) period in comparison to the cumulative ETF (2023 – 2020) period (Figure 3). Additionally, the cumulative ETF period showed higher levels of erosion towards the heads of the channels than the delayed ETF period.

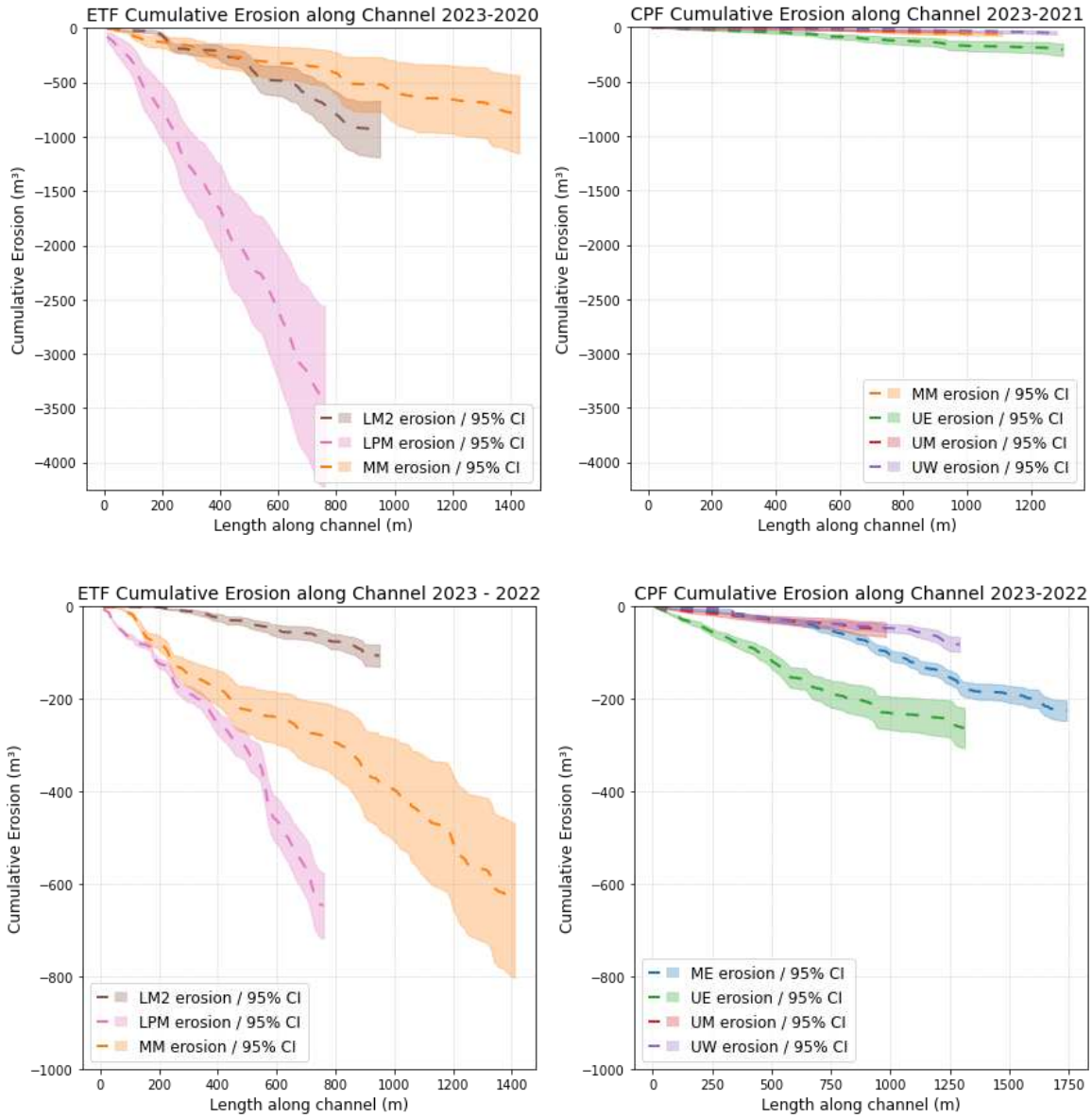

Figure 3 (Top Left) Cumulative erosion values along the channel with 95% confidence intervals in ETF study areas for the cumulative 2023 – 2020 DoD. The length along channel axis starts at the most upstream end of the study area. (Top Right) Cumulative erosion values along the channel in CPF study areas for the cumulative 2023 – 2021 DoD. (Bottom Left) Cumulative erosion values along the channel in ETF study areas for the delayed 2023 – 2022 DoD. (Bottom Right) Cumulative erosion values along the channel in CPF study areas for the delayed 2023 – 2022 DoD.

Cumulative deposition along the channel was also higher in ETF study areas than CPF study areas (Figure 4). Analysis of net sediment change indicated that ETF areas were predominantly erosional. In contrast, CPF areas exhibited a more balanced distribution of erosion and deposition, making it unclear whether these areas were net erosional or depositional.

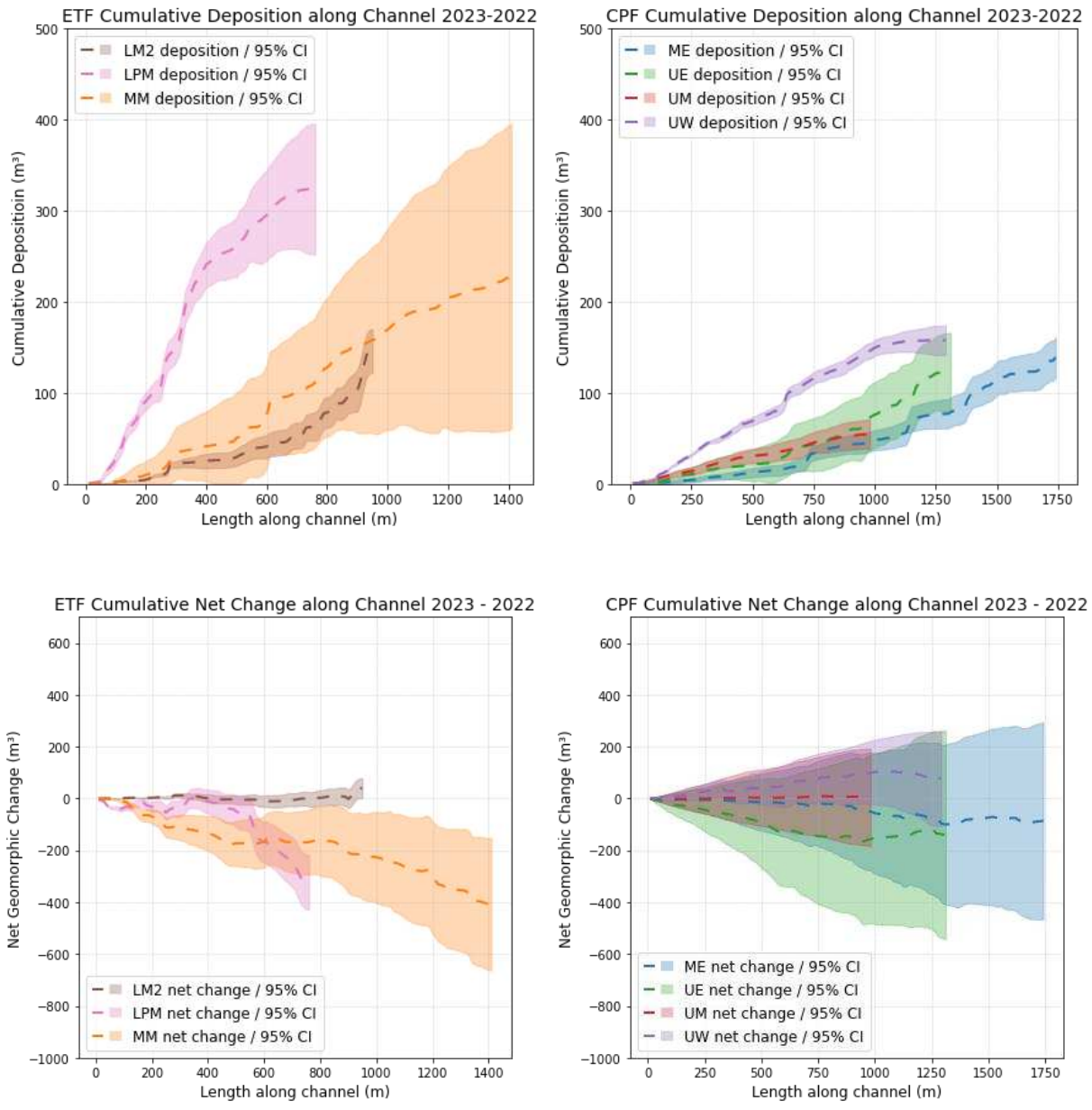

Figure 4 (Top Left) Cumulative deposition values with 95% confidence intervals in ETF study areas for the delayed 2023 – 2022 DoD. The length along channel axis starts at the most

upstream end of the study area. (Top Right) Cumulative deposition values in CPF study areas for the delayed 2023 – 2022 DoD. (Bottom Left) Cumulative net change along the channel in ETF study areas for the delayed 2023 – 2022 DoD. (Bottom Right) Cumulative net change along the channel in CPF study areas for the delayed 2023 – 2022 DoD.

3.2 **Cumulative Erosion (2023–2021/2020)**

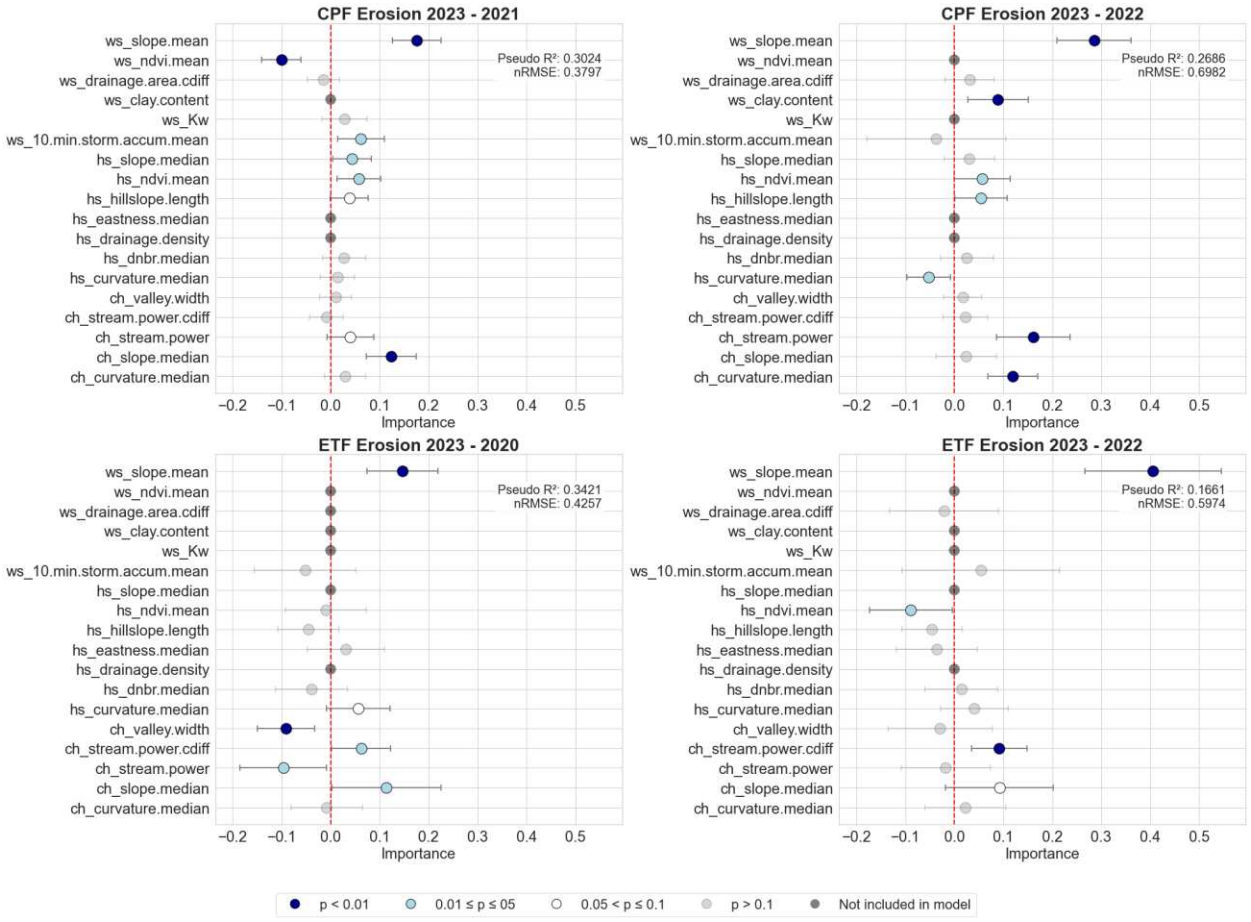

Figure 5. SSN model results for the Erosion 2023 – 2021/2020 dependent variable. Pseudo R^2 indicates the proportion of variance explained by the predictors, while nRMSE indicates model performance (lower is better). The error bars are the 95% confidence interval produced internally by the model.

In the erosion 2023-2021 models, watershed slope (*ws_slope.mean*) and channel slope (*ch_slope.median*) had predominantly positive coefficients across both burn scars, while hillslope slope (*hs_slope.median)* was found to be significantly positively correlated with erosion in the CPF-combined model, but not the ETF-combined model (Figure 5, Table B2). Stream power (*ch_stream.power)* was consistently positively correlated with erosion in both the CPF-combined and three of the four CPF-individual models, whereas the ETF-combined model showed negative correlations.

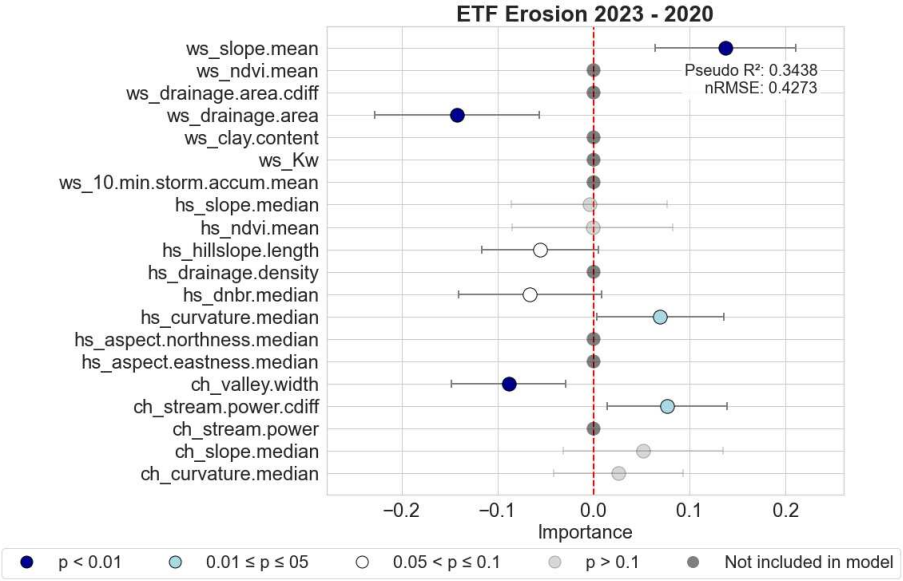

Figure 6. SSN model results for ETF-combined erosion 2023-2020, with watershed drainage area (*ws_drainage.area*) substituted in place of *ch_stream.power.* Erosion in this timestep also negatively correlated with *ws_drainage.area* as well as *ch_stream.power*, indicating that in the ETF study areas, higher levels of erosion are more likely to occur higher up in the basin.

Precipitation (*ws_10.min.storm.accum.mean)* was modestly positive in the CPF-combined model (0.06, $p < 0.05$), but insignificant in the ETF-combined model, indicating short-duration intense rainfall slightly increased erosion.

In the CPF-combined model, hillslope NDVI (*hs_ndvi.mean)* showed a positive association with erosion, while watershed NDVI (*ws_ndvi.mean*), displayed a negative association. Hillslope dNBR (*hs_dnbr.mean)* didn't significantly predict erosion in either the CPF- or ETF-combined models. None of the ETF-combined or individual models showed vegetation or soils independent variables as significant factors in predicting erosion. The ETF-combined model showed significant negative correlation with valley width (*ch_valley.width)* while the CPF-combined model showed no significant correlation.

3.3 **Delayed Erosion (2023–2022)**

Watershed slope (*ws_slope.mean*) was again found to be a strong significant predictor in both the CPF-combined (0.29, $p < 0.01$) and ETF-combined (0.41, $p < 0.01$) delayed erosion (2023 - 2022) models (Figure 5 & Table B3). Channel stream power (*ch_stream.power)* positively influenced erosion in CPF-combined (0.16, $p < 0.05$), while channel slope (*ch_slope.median)* positively influenced erosion in the ETF-combined models. Hillslope slope (*hs_slope.median*) was not found to significantly correlate with erosion in either burn scar.

Non-slope related topographic variables were generally more significant in the CPF models and less important in the ETF models. Channel-scale curvature (*ch_curvature.median)* positively predicted erosion in CPF-combined (0.12, $p < 0.01$) and two of the CPF-individual models, suggesting the reaches with a concave profile increased erosion. Conversely, hillslope-scale curvature *(hs_curvature.median*) was negatively associated in CPF-combined (–0.05, $p < 0.05$)

and two individual models, suggesting that channels with contributing hillslopes with a concave profile experienced less erosion. Valley width (*ch_valley.width)* was not found to significantly influence erosion in either of the combined models, although larger valley widths showed a negative correlation with erosion in two of the CPF-individual models.

Vegetation and soil predictors exhibited mixed influences, with NDVI *(hs_ndvi.mean*) positively correlated with erosion in the CPF-combined model (0.06, $p < 0.05$) but negatively correlated in the ETF-combined (–0.09, $p < 0.05$). Clay content (*ws_clay.content*) showed a positive association in CPF-combined (0.09, $p < 0.05$). Storm accumulation was found to be non-significant in both combined models.

3.4 Delayed Deposition (2023–2022)

Topographic and slope-related variables showed the most significant influence on delayed deposition (2023 – 2022) SSN models for both CPF and ETF burn scars, but the direction of their influence varied by study area (Figure 7 & Table B1). In CPF-individual models, slope at the channel, hillslope, and watershed scales consistently emerged as a significant negative predictor. Median channel slope (*ch_slope.median*) showed negative correlations with deposition in the CPF-combined model (–0.18, $p < 0.01$) as well as a three of the four CPF-individual models, suggesting that steeper slopes correspond to reduced deposition in the CPF burn scar both within each study area as well as across study areas. Conversely, in the ETF burn scar, slope variables generally exhibited positive relationships with deposition, notably *ch_slope.median*, with highly significant positive coefficients in the ETF-combined model (0.33, $p < 0.05$) as well as two of the three ETF-individual models. Figure 9 shows evidence of deposition in reaches with high slope due to bank failure.

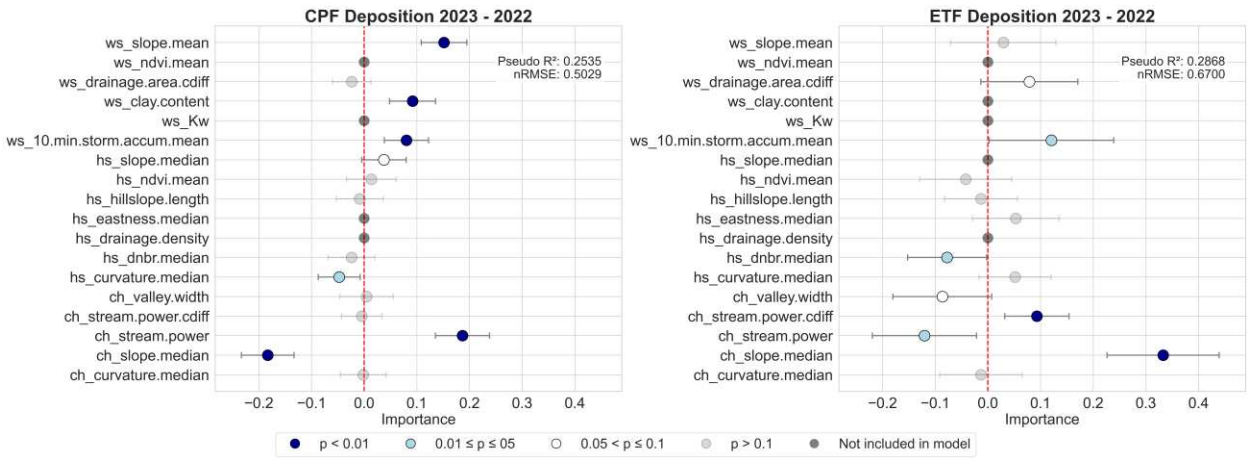

Figure 7. SSN model results for the Deposition 2023 – 2022 dependent variable. Pseudo R^2 indicates the proportion of variance explained by the predictors, while nRMSE indicates model performance. The error bars are the 95% confidence interval produced internally by the model.

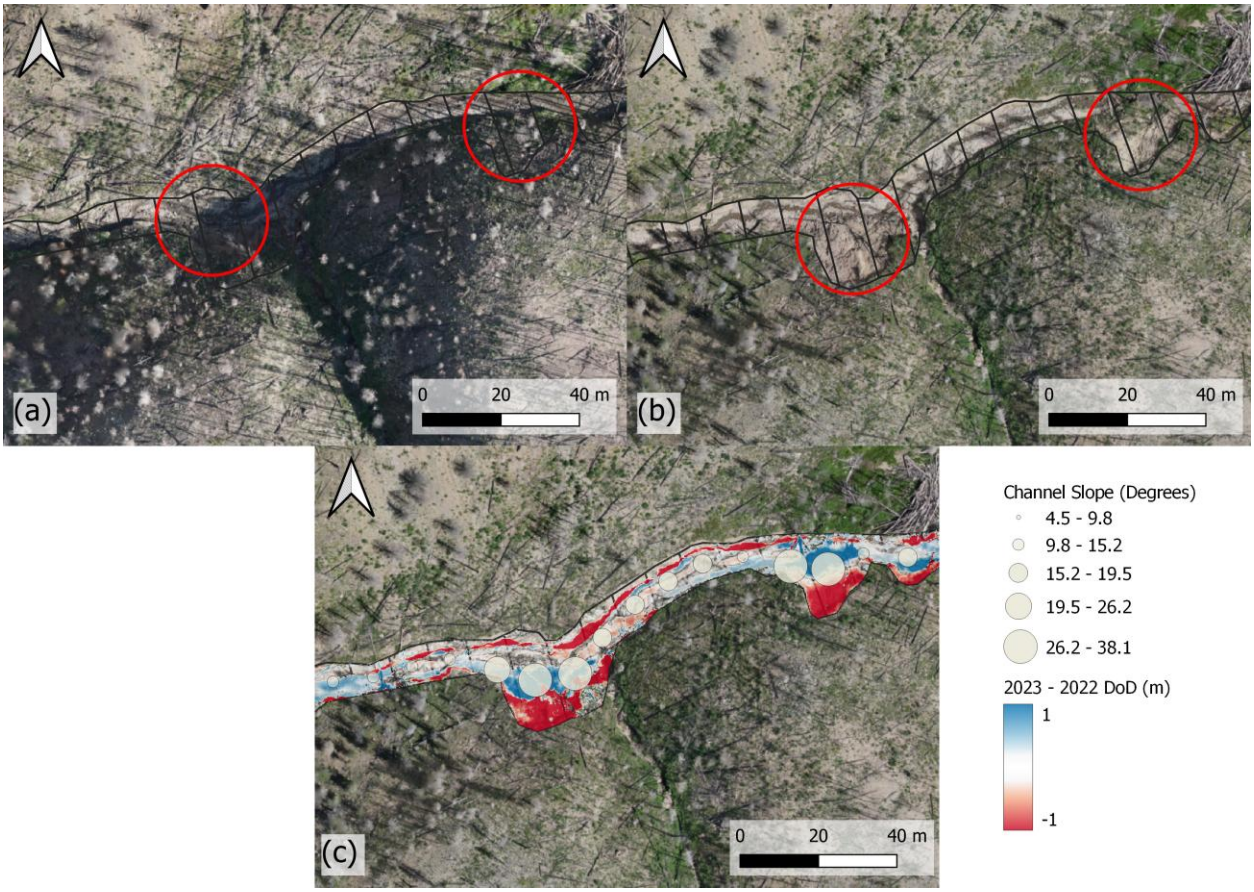

Figure 8. High deposition in reaches with high slope due to bank erosion in the ETF-LPM study area. a) 2022 orthomosaic image, with banks circled in red b) 2023 orthomosaic image with eroded banks circled in red c) DoD showing high deposition in reaches that have high slope.

Channel stream power (*ch_stream.power*) was found to be significantly negatively correlated with deposition in the ETF-combined model (-0.12, $p < 0.05$) and significantly positively correlated in the CPF-combined model (0.19, $p < 0.01$) as well as two of the four CPF-individual models. Figure 9 below shows that when basin area (*ws_drainage.area)* is included in the model in place of *ch_stream.power,* it is also positively correlated with deposition in the CPF-combined model.

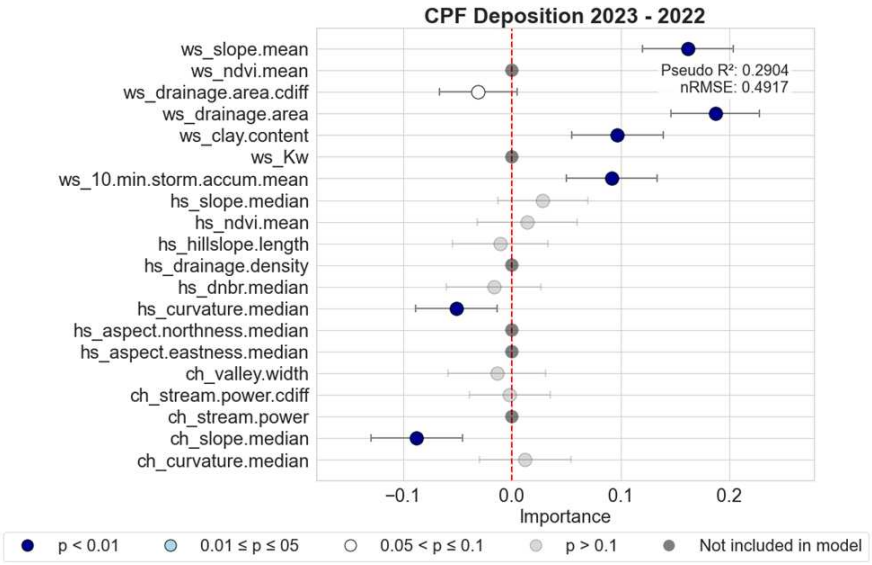

Figure 9. SSN model results for CPF-combined deposition 2023-2022, with watershed drainage area (ws_drainage.area) substituted in place of ch_stream.power. Deposition in this timestep is positively correlated with ws_drainage.area as well as ch_stream.power, indicating that in the CPF study areas, higher levels of deposition are more likely to occur in reaches with higher basin areas.

Precipitation, measured as mean 10-minute storm accumulation (*ws_10.min.storm.accum.mean),* consistently had modest positive coefficients (CPF-combined: 0.08, $p < 0.01$; ETF-combined: 0.12, $p < 0.05$), suggesting slightly increased deposition associated with higher storm accumulations. Vegetation and soil predictors, such as median dNBR *(hs_dnbr.median*) and mean NDVI (*hs_ndvi.mean),* appeared less frequently, contributing minor positive or negative effects when retained. Clay content *(ws_clay.content*) was retained only in CPF-combined (0.09, $p < 0.01$).

Other non-slope-related topography variables showed mixed relationships in both burn scars. Valley width (*ch_valley.width)* showed a positive correlation with deposition in the ETF-

combined model (0.13, $p < 0.05$) and no significance in the ETF-individual models, while it showed no significance in the CPF-combined model and mixed relationships in the CPF-individual models. Drainage area changes (*ws_drainage.area.cdiff*), which indicate confluences, exhibited small and variable coefficients with no consistent direction across study areas. Curvature metrics such as median channel curvature (*ch_curvature.median*) had weaker and inconsistent relationships that were often lacking statistical significance.

3.5 **Delayed Net Change (2023–2022)**

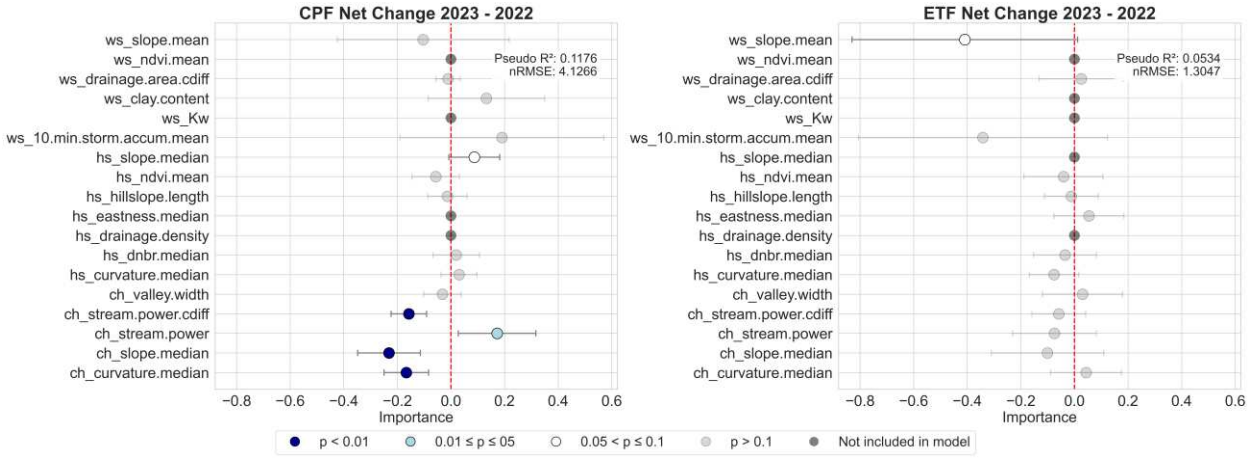

Figure 10. SSN model results for the Net Change 2023 – 2022 dependent variable. Pseudo R^2 indicates the proportion of variance explained by the predictors, while nRMSE indicates model performance. The error bars are the 95% confidence interval produced internally by the model.

The net change (2023 – 2022) models for the CPF and ETF burn scars performed notably worse than all the erosion and deposition models, with nRMSE scores for both combined models significantly greater than 1. (Figure 10 & Table B4). These results indicate that the models performed worse than a baseline prediction using the mean observed value of net change, suggesting that they do not adequately capture the processes driving net geomorphic change in

the channel. The CPF-combined net change model was the only combined model across dependent variables and burn scars that found *ws_slope.mean* to be an insignificant predictor, although *ch_slope.median* (-0.23, $p < 0.01$) was found to significantly increase the magnitude of erosion relative to deposition within a reach. In the ETF-combined net change model, *ws_slope.mean* (-0.41, $p < 0.1$) was the only significant predictor, with increases in contributing area slope being associated with increased relative erosion. In CPF-combined, positive coefficients for *ch_stream.power* (0.17, $p < 0.05$) and *hs_slope.median* (0.09, $p < 0.1$) indicated that higher contributing hillslope gradient and stream power were associated with greater deposition in a reach relative to erosion.

4. DISCUSSION

4.1 Dominant Predictor Variables Between Burn Scars

Across all models, topographic controls governed post-wildfire sediment dynamics, but their effects diverged between CPF and ETF burn scars. We found that topographic slope—measured at channel and watershed scales—was the strongest predictor of both erosion and deposition. In the CPF burn scar, steeper channel gradients reduced deposition and amplified erosion, consistent with theory linking high slopes to greater transport capacity and limited storage. In contrast, steeper gradients in ETF increased both erosion and deposition. Orthomosaic imagery in Figure 7 revealed bank failures in several high-slope reaches of ETF, which supplied sediment and produced the unexpected positive correlation between *ch_slope.median* and deposition. The reliance on remotely sensed datasets limits the ability to directly assess historical channel morphology or legacy features, such as prior debris flow deposits, that may influence current sediment availability and channel response. Without detailed field-based stratigraphic data, it

remains uncertain how much of the observed sediment supply is attributable to post-fire processes versus remobilization of pre-existing deposits.

Channel stream power (*ch_stream.power*) correlated negatively with deposition and positively with erosion in most models. However, in the delayed CPF-combined (2022–2023) model it showed a positive correlation with deposition, and in the cumulative ETF-combined (2020–2023) model it showed a negative correlation with erosion. Because stream power integrates basin area, slope, and channel width, interpretation issues may arise due to correlated predictors. Specifically, omitting watershed area can bias the estimated influence of stream power, potentially exaggerating or understating its true effect on geomorphic change. When we substituted drainage area (ws_drainage.area) directly into these two models, basin area emerged as a stronger driver of reach-scale deposition in the delayed CPF model and reach-scale erosion in the cumulative ETF model, compared to slope or channel width. So while stream power initially appeared as a dominant factor, part of this apparent dominance may reflect the unmodeled influence of watershed area.

The role of precipitation emerged as a secondary but notable predictor, particularly in the CPF burn scar. Higher short-duration storm accumulations modestly enhanced both deposition and erosion, likely reflecting increased runoff and sediment delivery following wildfire-induced vegetation loss and reduced infiltration. This influence was less apparent in ETF models, potentially due to the lower relative amount and intensity of precipitation in the ETF study areas compared to the CPF study areas (Figure 11). Additionally, the lack of statistical significance of the 10-minute storm accumulation predictor in some models may reflect limited variation in precipitation accumulation across watersheds within each burn scar, which reduces the statistical power to detect associations with geomorphic response.

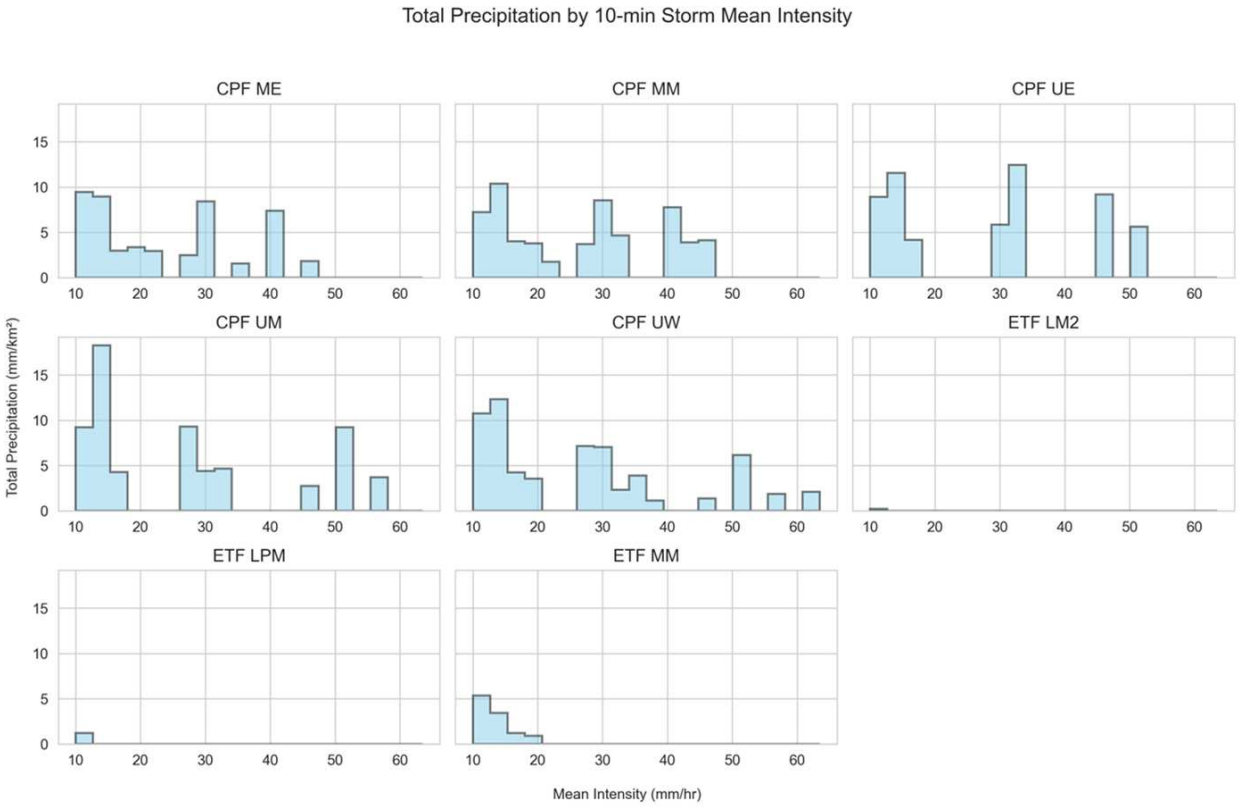

Figure 11. Storm accumulation for precip > 10 mm/hr intensity CPF study areas (May to October, May 1st 2021 to June 1st 2023) and ETF study areas (May to October, May 1st 2021 to July 9th, 2023). CPF watersheds show significantly higher volumes of high intensity storms than ETF watersheds.

Vegetation metrics, including NDVI and burn severity (dNBR), exhibited limited explanatory power, with sporadic statistical significance and variable directional relationships. This limited effect may reflect complex interactions between vegetation recovery patterns and geomorphic processes that are not adequately captured by these metrics alone. It may also be due to limited variation in these metrics within the study watersheds, which reduces their ability to explain differences in erosion despite their known importance in post-fire geomorphic response. Similarly, soil texture variables, such as clay content, provided minor and inconsistent contributions, emphasizing the overriding influence of topographic factors.

In general, watershed and channel scale predictors were more often found to be significant than hillslope scale predictors. Slope metrics at watershed, channel, and hillslope scales consistently dominated as the primary predictors of both erosion and deposition. Watershed-scale slope was notably the strongest predictor of erosion across burn scars, with channel-scale slope relationships also often significant and high in magnitude across models. Hillslope gradient was most inconsistent of the slope terms, with weak positive relationships found in the CPF-combined erosion and deposition models, but not in any of the ETF-combined models.

Curvature and valley geometry exerted secondary, scale-specific influences. Channels with a concave curvature promoted erosion in CPF watersheds, whereas hillslopes with a convex curvature were correlated with increase erosion in the channels below. Valley width positively influenced deposition and negatively affected erosion in ETF watersheds, though it showed limited significance in CPF.

The predictive models for net change in both burn scars exhibited limited performance, with nRMSE values exceeding 1, indicating predictions no better than random chance. One explanation for this poor performance arises from the statistical characteristics of the data. Specifically, net sediment change data typically cluster closely around zero due to balanced erosion and deposition across many channel segments, while a smaller subset of segments experience predominantly erosional or depositional conditions. These few extreme segments act as outliers, inflating prediction errors in a dataset otherwise narrowly distributed around zero. Additionally, the approach of summarizing erosion, deposition, and net change over uniform 10-meter channel segments ignores inherent geomorphic variability. This segmentation strategy does not account for underlying geomorphic process units, such as riffles, pools, or step pools. Consequently, individual segments may contain mixed process domains that experience

opposing sediment dynamics, potentially complicating the interpretation of net erosion or deposition at the segment scale.

4.2 Cumulative and Delayed Erosion Responses

Topographic variables consistently emerged as the dominant controls on erosion, but their relative importance and specific roles evolved between the cumulative (2023 – 2021 for CPF, 2023 – 2020 for ETF) and delayed (2023 – 2022) periods. Watershed slope was a primary driver of erosion during both periods, exhibiting significant positive correlations in the CPF and ETF combined models. Channel slope a common driver in both the cumulative and delayed ETF models. In the CPF-combined cumulative model, both hillslope and channel slopes were positively correlated with erosion, but neither variable remained significant in the delayed period.

Channel stream power was positively correlated with erosion in the CPF models across both timeframes, as expected. In contrast, it was negatively correlated in the cumulative ETF model and not significant in the delayed ETF model—suggesting that more erosion occurred in upstream reaches immediately following fire. This pattern may reflect post-fire channel head migration, as described by Wohl & Scott (2017), where it was shown that increased runoff and reduced infiltration can trigger upslope migration of channel heads by lowering the threshold contributing area for channel initiation. As vegetation recovers and hydrologic function is restored, these channel heads often retreat downslope. It is plausible that this transient shift in channel head position contributed to elevated erosion in upper portions of the ETF watersheds shortly after the fire, with a subsequent reduction in erosion by 2022. This hypothesis is supported by the increased significance of hillslope NDVI (*hs_ndvi.mean*) in the delayed ETF-

combined model relative to the cumulative model, indicating that as vegetation recovered on the hillslopes adjacent to channels, erosion decreased.

Storm accumulation exhibited a modest but significant influence on erosion during the cumulative CPF-combined period, suggesting that short-duration intense rainfall events have the highest importance in driving erosional responses in the channel closely following the fire. Notably, precipitation remained insignificant in the ETF models, potentially due to the lower levels of storm accumulation in the ETF study areas relative to the CPF study areas. Another explanation for the lack of significance in storm accumulation could be attributed to the coarse, 1-kilometer spatial resolution of the MRMS precipitation data, which may be mischaracterizing the intensity of summer thunderstorms less than the size of a MRMS pixel. Additionally, because the analysis relies on cumulative multi-event averages, the geomorphic significance of individual, high-intensity storm events may be underrepresented. Isolated storm-driven events can drive substantial erosion or deposition that is not fully captured by aggregated metrics, potentially leading to conservative estimates of storm-scale responses.

Clay content showed a significant moderate correlation with erosion in the CPF-combined delayed model, but not in the cumulative model, suggesting that reduced infiltration in high clay soils could be driving more erosive flows in the channels. The consistent positive correlation between NDVI and erosion in the cumulative and delayed CPF-combined models potentially indicates that hillslopes with high vegetative cover may also have higher soil moisture, receive higher amounts of rainfall, or have some other factor that contributes to higher erosive flows in the channels below. Storm

Interestingly, burn severity metrics (dNBR) did not emerge as significant predictors of erosion in either burn scar during the cumulative or delayed erosion periods. This finding highlights the

complexity of post-fire erosion dynamics and suggests that metrics of immediate burn severity may not directly translate into predictive indicators of geomorphic change at these temporal scales.

5. CONCLUSION

Our study demonstrates that post-wildfire sediment dynamics in CPF and ETF burn scars are primarily controlled by topographic factors, particularly channel and watershed slopes. In CPF, steeper gradients predominantly facilitated erosion and limited deposition, aligning with traditional sediment transport theory. Conversely, in ETF, steeper slopes had dual effects—promoting both erosion and deposition—primarily through localized sediment inputs from bank failures, highlighting the necessity for targeted slope stabilization strategies in similar contexts.

Precipitation emerged as a secondary predictor, with its significance likely constrained by both the limited variability of storm accumulation across watersheds and the resolution of available precipitation data. In CPF watersheds, higher short-duration storm totals showed modest associations with increased erosion and deposition; however, the narrow range of precipitation values likely reduced statistical power to detect stronger relationships. In ETF watersheds, lower storm intensities and limited spatial variability contributed to the absence of significant precipitation effects. Additionally, the coarse 1-km resolution of MRMS data may have failed to capture localized, high-intensity convective storms that disproportionately influence sediment dynamics. The reliance on cumulative, multi-event precipitation metrics further diluted the influence of individual extreme events, introducing additional challenges in quantifying the role of precipitation in post-fire geomorphic responses. Conversely, vegetation recovery indicators

(NDVI, burn severity) were inconsistent predictors, suggesting these variables have limited standalone explanatory power and interact complexly with broader geomorphic processes.

Additionally, our findings indicate that in ETF watersheds, erosion was more prominent in upstream reaches during the cumulative post-fire period, but this pattern did not persist into the delayed period. This suggests a transient upslope shift in erosional activity immediately following the fire, potentially driven by changes in hydrologic connectivity and channel initiation thresholds. As hydrologic function recovered and vegetation reestablished, these upstream contributions diminished, leading to reduced erosion in higher elevations by 2022.

Future work should prioritize examining specific mechanisms driving slope-related sediment contributions, exploring interactions between topographic factors and vegetation recovery, and quantifying precipitation intensity thresholds that trigger substantial geomorphic changes. These insights would improve predictive frameworks and guide effective post-fire watershed management. The limitations inherent in the current analysis, including reliance on multi-event averages, may mask critical variability and diminish recognition of the geomorphic significance of individual storm events. Furthermore, the exclusive use of remotely sensed datasets precludes consideration of historical channel morphology evolution, such as legacy debris flow deposits, which can significantly influence contemporary channel dynamics. Incorporating these considerations into future studies will be essential for a more comprehensive understanding of post-fire geomorphic processes.

REFERENCES

Anderson, S. W. (2019). Uncertainty in quantitative analyses of topographic change: error propagation and the role of thresholding. *Earth Surface Processes and Landforms*, *44*(5), 1015–1033. https://doi.org/10.1002/esp.4551

Benavides-Solorio, J. de D., & MacDonald, L. H. (2005). Measurement and prediction of post-fire erosion at the hillslope scale, Colorado Front Range. *International Journal of Wildland Fire*, *14*(4), 457–474. https://doi.org/10.1071/WF05042

Benda, L., Miller, D., Bigelow, P., & Andras, K. (2003). Effects of post-wildfire erosion on channel environments, Boise River, Idaho. *Forest Ecology and Management*, *178*(1–2), 105–119. https://doi.org/10.1016/S0378-1127(03)00056-2

Bradford, J. M., Ferris, J. E., & Remley, P. A. (1987). Interrill Soil Erosion Processes: I. Effect of Surface Sealing on Infiltration, Runoff, and Soil Splash Detachment. *Soil Science Society of America Journal*, *51*(6), 1566–1571. https://doi.org/10.2136/sssaj1987.03615995005100060029x

Brasington, J., & Smart, R. M. A. (2003). Close range digital photogrammetric analysis of experimental drainage basin evolution. *Earth Surface Processes and Landforms*, *28*(3), 231–247. https://doi.org/10.1002/esp.480

Brogan, D. J., Nelson, P. A., & MacDonald, L. H. (2019). Spatial and temporal patterns of sediment storage and erosion following a wildfire and extreme flood. *Earth Surface Dynamics*, *7*(2), 563–590. https://doi.org/10.5194/esurf-7-563-2019

Bull, W. B. (1979). Threshold of critical power in streams. *GSA Bulletin*, *90*(5), 453–464. https://doi.org/10.1130/0016-7606(1979)90<453:TOCPIS>2.0.CO;2

Burnham, K. P., Anderson, D. R., & Anderson, D. R. (2010). *Model selection and multimodel inference: a practical information-theoretic approach* (2. ed., [4. printing]). New York, NY: Springer.

Cannon, S. H., & DeGraff, J. (2009). The Increasing Wildfire and Post-Fire Debris-Flow Threat in Western USA, and Implications for Consequences of Climate Change. In K. Sassa & P. Canuti (Eds.), *Landslides – Disaster Risk Reduction* (pp. 177–190). Berlin, Heidelberg: Springer. https://doi.org/10.1007/978-3-540-69970-5_9

Chapman, S. S., Griffith, G. E., Omernik, J. M., Price, A. B., Freeouf, J., & Schrupp, D. L. (2006). Ecoregions of Colorado. Reston, Virginia: U.S. Geological Survey.

Chirico, P., DeWitt, J., & Bergstresser, S. (2020). Evaluating Elevation Change Thresholds between Structure-from-Motion DEMs Derived from Historical Aerial Photos and 3DEP LiDAR Data. *Remote Sensing*, *12*(10), 1625. https://doi.org/10.3390/rs12101625

Clark, A., Moorman, B., Whalen, D., & Fraser, P. (2021). Arctic coastal erosion: UAV-SfM data collection strategies for planimetric and volumetric measurements. *Arctic Science*, *7*(3), 605–633. https://doi.org/10.1139/as-2020-0021

Cook, K. L., & Dietze, M. (2019). Short Communication: A simple workflow for robust low-cost UAV-derived change detection without ground control points. *Earth Surface Dynamics*, *7*(4), 1009–1017. https://doi.org/10.5194/esurf-7-1009-2019

DeBano, L., Neary, D., & Ffolliott, P. (1998). *Fire's Effects on Ecosystems*.

DeBano, L. F. (1981). *Water Repellent Soils: A State-of-the-art*. U.S. Department of Agriculture, Forest Service, Pacific Southwest Forest and Range Experiment Station.

Doerr, S. H., & Thomas, A. D. (2000). The role of soil moisture in controlling water repellency: new evidence from forest soils in Portugal. *Journal of Hydrology*, *231–232*, 134–147. https://doi.org/10.1016/S0022-1694(00)00190-6

Dumelle, M., Peterson, E. E., Ver Hoef, J. M., Pearse, A., & Isaak, D. J. (2024). SSN2: The next generation of spatial stream networkmodeling in R. *Journal of Open Source Software*, *9*(99), 6389. https://doi.org/10.21105/joss.06389

Esposito, G., Gariano, S. L., Masi, R., Alfano, S., & Giannatiempo, G. (2023). Rainfall conditions leading to runoff-initiated post-fire debris flows in Campania, Southern Italy. *Geomorphology*, *423*, 108557. https://doi.org/10.1016/j.geomorph.2022.108557

Fernández, C., Vega, J. A., & Vieira, D. C. S. (2010). Assessing soil erosion after fire and rehabilitation treatments in NW Spain: Performance of rusle and revised Morgan-Morgan-Finney models: ASSESSING SOIL EROSION AFTER FIRE. *Land Degradation & Development*, *21*(1), 58–67. https://doi.org/10.1002/ldr.965

Fuller, I. C. (2008). Geomorphic impacts of a 100-year flood: Kiwitea Stream, Manawatu catchment, New Zealand. *Geomorphology*, *98*(1), 84–95. https://doi.org/10.1016/j.geomorph.2007.02.026

Gartner, J. E., Cannon, S. H., & Santi, P. M. (2014). Empirical models for predicting volumes of sediment deposited by debris flows and sediment-laden floods in the transverse ranges of southern California. *Engineering Geology*, *176*, 45–56. https://doi.org/10.1016/j.enggeo.2014.04.008

Goode, J. R., Luce, C. H., & Buffington, J. M. (2012). Enhanced sediment delivery in a changing climate in semi-arid mountain basins: Implications for water resource management and

aquatic habitat in the northern Rocky Mountains. *Geomorphology*, *139–140*, 1–15. https://doi.org/10.1016/j.geomorph.2011.06.021

de Haas, T., Nijland, W., McArdell, B. W., & Kalthof, M. W. M. L. (2021). Case Report: Optimization of Topographic Change Detection With UAV Structure-From-Motion Photogrammetry Through Survey Co-Alignment. *Frontiers in Remote Sensing*, *2*. Retrieved from https://www.frontiersin.org/articles/10.3389/frsen.2021.626810

Hayter, L. (2023). Evaluating Post-Fire Geomorphic Change on Paired Mulched and Unmulched Watersheds using Repeat Drone Surveys.

Horton, R. E. (1945). Erosional Development Of Streams And Their Drainage Basins; Hydrophysical Approach To Quantitative Morphology. *GSA Bulletin*, *56*(3), 275–370. https://doi.org/10.1130/0016-7606(1945)56[275:EDOSAT]2.0.CO;2

Hugonnet, R., McNabb, R., Berthier, E., Menounos, B., Nuth, C., Girod, L., et al. (2021). Accelerated global glacier mass loss in the early twenty-first century. *Nature*, *592*(7856), 726–731. https://doi.org/10.1038/s41586-021-03436-z

Inbar, M., Tamir, M., & Wittenberg, L. (1998). Runoff and erosion processes after a forest fire in Mount Carmel, a Mediterranean area. *Geomorphology*, *24*(1), 17–33. https://doi.org/10.1016/S0169-555X(97)00098-6

Istanbulluoglu, E., & Bras, R. L. (2006). On the dynamics of soil moisture, vegetation, and erosion: Implications of climate variability and change. *Water Resources Research*, *42*(6), 2005WR004113. https://doi.org/10.1029/2005WR004113

Jackson, M., & Roering, J. J. (2009). Post-fire geomorphic response in steep, forested landscapes: Oregon Coast Range, USA. *Quaternary Science Reviews*, *28*(11–12), 1131–1146. https://doi.org/10.1016/j.quascirev.2008.05.003

James, M., Stuart Robson, & Mark W. Smith. (2017). 3-D uncertainty-based topographic change detection with structure-from-motion.pdf.

James, M. R., & Robson, S. (2014). Mitigating systematic error in topographic models derived from UAV and ground-based image networks. *Earth Surface Processes and Landforms*, *39*(10), 1413–1420. https://doi.org/10.1002/esp.3609

James, M. R., Antoniazza, G., Robson, S., & Lane, S. N. (2020). Mitigating systematic error in topographic models for geomorphic change detection: accuracy, precision and considerations beyond off-nadir imagery. *Earth Surface Processes and Landforms*, *45*(10), 2251–2271. https://doi.org/10.1002/esp.4878

Kampf, S. K., Brogan, D. J., Schmeer, S., MacDonald, L. H., & Nelson, P. A. (2016). How do geomorphic effects of rainfall vary with storm type and spatial scale in a post-fire landscape? *Geomorphology*, *273*, 39–51. https://doi.org/10.1016/j.geomorph.2016.08.001

Kirkby, M. J., & Cox, N. J. (1995). A climatic index for soil erosion potential (CSEP) including seasonal and vegetation factors. *CATENA*, *25*(1–4), 333–352. https://doi.org/10.1016/0341-8162(95)00016-L

Lane, P. N. J., Sheridan, G. J., & Noske, P. J. (2006). Changes in sediment loads and discharge from small mountain catchments following wildfire in south eastern Australia. *Journal of Hydrology*, *331*(3), 495–510. https://doi.org/10.1016/j.jhydrol.2006.05.035

Langbein, W. B., & Schumm, S. A. (1958). Yield of sediment in relation to mean annual precipitation. *Eos, Transactions American Geophysical Union*, *39*(6), 1076–1084. https://doi.org/10.1029/TR039i006p01076

Larsen, I. J., & MacDonald, L. H. (2007). Predicting postfire sediment yields at the hillslope scale: Testing RUSLE and Disturbed WEPP. *Water Resources Research*, *43*(11), 2006WR005560. https://doi.org/10.1029/2006WR005560

Leopold, L. B., & Maddock, T. (1953). *The Hydraulic Geometry of Stream Channels and Some Physiographic Implications*. U.S. Government Printing Office.

Lindsay, J. B. (2014). The Whitebox Geospatial Analysis Tools Project and Open-Access GIS. *Proceedings of the GIS Research UK 22nd Annual Conference, He University of Glasgow*.

McGuire, L. A., Ebel, B. A., Rengers, F. K., Vieira, D. C. S., & Nyman, P. (2024). Fire effects on geomorphic processes. *Nature Reviews Earth & Environment*, *5*(7), 486–503. https://doi.org/10.1038/s43017-024-00557-7

Melton, M. A. (1957). *AN ANALYSIS OF THE RELATIONS AMONG ELEMENTS OF CLIMATE, SURFACE PROPERTIES, AND GEOMORPHOLOGY:* Fort Belvoir, VA: Defense Technical Information Center. https://doi.org/10.21236/AD0148373

Montgomery, D. R., & Dietrich, W. E. (1989). Source areas, drainage density, and channel initiation. *Water Resources Research*, *25*(8), 1907–1918. https://doi.org/10.1029/WR025i008p01907

Moody, J. A. (2001). SEDIMENT TRANSPORT REGIMES AFTER A WILDFIRE IN STEEP MOUNTAINOUS TERRAIN. Presented at the Proceedings of the Seventh Federal Interagency Sedimentation Conference.

Moody, J. A., & Kinner, D. A. (2006). Spatial structures of stream and hillslope drainage networks following gully erosion after wildfire. *Earth Surface Processes and Landforms*, *31*(3), 319–337. https://doi.org/10.1002/esp.1246

Moody, J. A., & Martin, D. A. (2001). Initial hydrologic and geomorphic response following a wildfire in the Colorado Front Range. *Earth Surface Processes and Landforms*, *26*(10), 1049–1070. https://doi.org/10.1002/esp.253

Moody, J. A., Martin, D. A., & Cannon, S. H. (2008). Post-wildfire erosion response in two geologic terrains in the western USA. *Geomorphology*, *95*(3), 103–118. https://doi.org/10.1016/j.geomorph.2007.05.011

Moore, I. D., & Burch, G. J. (1986). Physical Basis of the Length-slope Factor in the Universal Soil Loss Equation. *Soil Science Society of America Journal*, *50*(5), 1294–1298. https://doi.org/10.2136/sssaj1986.03615995005000050042x

Murphy, S. F., Writer, J. H., McCleskey, R. B., & Martin, D. A. (2015). The role of precipitation type, intensity, and spatial distribution in source water quality after wildfire. *Environmental Research Letters*, *10*(8), 084007. https://doi.org/10.1088/1748-9326/10/8/084007

Murray, J. T. (2023). Large-Scale Remote Sensing of Geomorphic Change In Mulched and Unmulched Watersheds Burned in the 2020 East Troublesome Fire, Colorado.

Niculiță, M., Mărgărint, M. C., & Tarolli, P. (2020). Chapter 10 - Using UAV and LiDAR data for gully geomorphic changes monitoring. In P. Tarolli & S. M. Mudd (Eds.), *Developments in Earth Surface Processes* (Vol. 23, pp. 271–315). Elsevier. https://doi.org/10.1016/B978-0-444-64177-9.00010-2

NRCS, U. (2021). Web Soil Survey. Retrieved November 1, 2024, from https://websoilsurvey.sc.egov.usda.gov/

Over, Ritchie, & Kranenburg. (2021). *Processing coastal imagery with Agisoft Metashape Professional Edition, version 1.6—Structure from motion workflow documentation* (Open-File Report).

Owens, P. N., Giles, T. R., Petticrew, E. L., Leggat, M. S., Moore, R. D., & Eaton, B. C. (2013). Muted responses of streamflow and suspended sediment flux in a wildfire-affected watershed. *Geomorphology*, *202*, 128–139. https://doi.org/10.1016/j.geomorph.2013.01.001

Patton, P. C., & Schumm, S. A. (1975). Gully Erosion, Northwestern Colorado: A Threshold Phenomenon. *Geology*, *3*(2), 88–90. https://doi.org/10.1130/0091-7613(1975)3<88:GENCAT>2.0.CO;2

Peterson, E. E., & Pearse, A. (2024). Correcting topological errors using SSNbler and QGIS.

PRISM Climate Group. (n.d.). PRISM Climate Group. Retrieved March 29, 2025, from http://prism.oregonstate.edu

Prosser, I. (1990). Fire, Humans and Denudation at Wangrah Creek, Southern Tablelands, N.S.W. *Australian Geographical Studies*, *28*(1), 77–95. https://doi.org/10.1111/j.1467-8470.1990.tb00623.x

Rengers, F. K., Tucker, G. E., Moody, J. A., & Ebel, B. A. (2016). Illuminating wildfire erosion and deposition patterns with repeat terrestrial lidar. *Journal of Geophysical Research: Earth Surface*, *121*(3), 588–608. https://doi.org/10.1002/2015JF003600

Rengers, F. K., McGuire, L. A., Kean, J. W., Staley, D. M., Dobre, M., Robichaud, P. R., & Swetnam, T. (2021). Movement of Sediment Through a Burned Landscape: Sediment Volume Observations and Model Comparisons in the San Gabriel Mountains, California,

USA. *Journal of Geophysical Research: Earth Surface*, *126*(7), e2020JF006053. https://doi.org/10.1029/2020JF006053

Rieke-Zapp, D. H., & Nearing, M. A. (2005). Slope Shape Effects on Erosion. *Soil Science Society of America Journal*, *69*(5), 1463–1471. https://doi.org/10.2136/sssaj2005.0015

Robichaud, P. R., Beyers, J. L., & Neary, D. G. (2000). *Evaluating the effectiveness of postfire rehabilitation treatments* (No. RMRS-GTR-63) (p. RMRS-GTR-63). Ft. Collins, CO: U.S. Department of Agriculture, Forest Service, Rocky Mountain Research Station. https://doi.org/10.2737/RMRS-GTR-63

Rolstad, C., Haug, T., & Denby, B. (2009). Spatially integrated geodetic glacier mass balance and its uncertainty based on geostatistical analysis: application to the western Svartisen ice cap, Norway. *Journal of Glaciology*, *55*(192), 666–680. https://doi.org/10.3189/002214309789470950

Shakesby, R. A. (2011). Post-wildfire soil erosion in the Mediterranean: Review and future research directions. *Earth-Science Reviews*, *105*(3), 71–100. https://doi.org/10.1016/j.earscirev.2011.01.001

Shean, D. E., Alexandrov, O., Moratto, Z. M., Smith, B. E., Joughin, I. R., Porter, C., & Morin, P. (2016). An automated, open-source pipeline for mass production of digital elevation models (DEMs) from very-high-resolution commercial stereo satellite imagery. *ISPRS Journal of Photogrammetry and Remote Sensing*, *116*, 101–117. https://doi.org/10.1016/j.isprsjprs.2016.03.012

Silva, F. C., Vieira, D. C. S., Van Der Spek, E., & Keizer, J. J. (2019). Effect of moss crusts on mitigation of post-fire soil erosion. *Ecological Engineering*, *128*, 9–17. https://doi.org/10.1016/j.ecoleng.2018.12.024

Staley, D., Wasklewicz, T., & Kean, J. (2010). Observations of drainage network change in a recently burned watershed using terrestrial laser scanning, *12*. Retrieved from https://pubs.usgs.gov/publication/70003766

US Forest Service. (2020a). *Cameron Peak Fire Forest Service Burned Area Emergency Response Executive Summary*. Arapaho Roosevelt National Forest.

US Forest Service. (2020b). *East Troublesome Fire Forest Service Burned Area Emergency Response Executive Summary*. Arapaho-Roosevelt and Medicine Bow-Routt National Forests.

USGS. (2022a, February). USGS CO NWCO 1 2020 & USGS CO NWCO 2 2020 (QL2) - LiDAR Mapping Report. The Sanborn Map Company, Inc.

USGS. (2022b, March). USGS CO Cameron Peak Fire 2021 - LiDAR Mapping Report. The Sanborn Map Company, Inc.

Ver Hoef, J. M., & Peterson, E. E. (2010). A Moving Average Approach for Spatial Statistical Models of Stream Networks. *Journal of the American Statistical Association*, *105*(489), 6–18. https://doi.org/10.1198/jasa.2009.ap08248

Ver Hoef, J. M., Peterson, E. E., Clifford, D., & Shah, R. (2014). **SSN** : An *R* Package for Spatial Statistical Modeling on Stream Networks. *Journal of Statistical Software*, *56*(3). https://doi.org/10.18637/jss.v056.i03

Vieira, D. C. S., Fernández, C., Vega, J. A., & Keizer, J. J. (2015). Does soil burn severity affect the post-fire runoff and interrill erosion response? A review based on meta-analysis of field rainfall simulation data. *Journal of Hydrology*, *523*, 452–464. https://doi.org/10.1016/j.jhydrol.2015.01.071

Wagenbrenner, J. W., Ebel, B. A., Bladon, K. D., & Kinoshita, A. M. (2021). Post-wildfire hydrologic recovery in Mediterranean climates: A systematic review and case study to identify current knowledge and opportunities. *Journal of Hydrology*, *602*, 126772. https://doi.org/10.1016/j.jhydrol.2021.126772

Wilson, C., Kampf, S. K., Wagenbrenner, J. W., & MacDonald, L. H. (2018). Rainfall thresholds for post-fire runoff and sediment delivery from plot to watershed scales. *Forest Ecology and Management*, *430*, 346–356. https://doi.org/10.1016/j.foreco.2018.08.025

Wischmeier, W. H., & Mannering, J. V. (1969). Relation of Soil Properties to its Erodibility. *Soil Science Society of America Journal*, *33*(1), 131–137. https://doi.org/10.2136/sssaj1969.03615995003300010035x

Wohl, E., & Scott, D. N. (2017). Transience of channel head locations following disturbance. *Earth Surface Processes and Landforms*, *42*(7), 1132–1139. https://doi.org/10.1002/esp.4124

Wohl, E. E., & Pearthree, P. P. (1991). Debris flows as geomorphic agents in the Huachuca Mountains of southeastern Arizona. *Geomorphology*, *4*(3), 273–292. https://doi.org/10.1016/0169-555X(91)90010-8

Workman, J. B., Cole, J. C., Shroba, R. R., Kellogg, K. S., & Premo, W. R. (2018). Geologic map of the Fort Collins 30'×60' quadrangle, Larimer and Jackson Counties, Colorado, and Albany and Laramie Counties, Wyoming. Reston, Virginia: U.S. Geological Survey.

Yochum, S. E., Sholtes, J. S., Scott, J. A., & Bledsoe, B. P. (2017). Stream power framework for predicting geomorphic change: The 2013 Colorado Front Range flood. *Geomorphology*, *292*, 178–192. https://doi.org/10.1016/j.geomorph.2017.03.004

Zuur, A.F., Ieno, E. N., & Saveliev, A. A. (2017). *Beginner's Guide to Spatial, Temporal and Spatial-Temporal Ecological Data Analysis with R-INLA* (Vol. I). Highland Statistics Ltd.

Zuur, Alain F., Ieno, E. N., & Elphick, C. S. (2010). A protocol for data exploration to avoid common statistical problems: *Data exploration*. *Methods in Ecology and Evolution*, *1*(1), 3–14. https://doi.org/10.1111/j.2041-210X.2009.00001.x